Probing the Core and Surface Composition of Base-Metal Nanoalloys to Rationalize their Selectivity: The Case of Ni-Fe/SiO 2 Catalysts for the Liquid-Phase Hydrogenation of Furfural

Dichao Shi, Achraf Sadier, Jean-Sébastien Girardon, Anne-Sophie Mamede, Carmen Ciotonea, Maya Marinova, Lorenzo Stievano, Moulay Sougrati, Camille La Fontaine, Sébastien Paul, et al.

Probing the Core and Surface Composition of Base-Metal Nanoalloys to Rationalize their Selectivity: The Case of Ni-Fe/SiO_2 Catalysts for the Liquid-Phase Hydrogenation of Furfural

Dichao Shi[1], Achraf Sadier[1], Jean-Sébastien Girardon[1], Anne-Sophie Mamede[1], Carmen Ciotonea[1†], Maya Marinova[2], Lorenzo Stievano[3], Moulay Tahar Sougrati[3], Camille La Fontaine[4], Sébastien Paul,[1] Robert Wojcieszak[1] and Eric Marceau[1]**

[1] Univ. Lille, CNRS, Centrale Lille, Univ. Artois, UMR 8181 – UCCS – Unité de Catalyse et Chimie du Solide, F-59000 Lille, France

[2] Univ. Lille, CNRS, INRAE, Centrale Lille, Univ. Artois, FR 2638-IMEC-Institut Michel-Eugène Chevreul, F-59000 Lille, France

[3] Institut Charles Gerhardt de Montpellier, UMR 5253, Université de Montpellier / CNRS / ENSCM, Pôle Chimie Balard Recherche CC 043 - 1919 route de Mende, F-34293 Montpellier Cedex 5, France

[4] Synchrotron SOLEIL, Beamline ROCK, L'Orme des Merisiers, F-91190 Saint-Aubin, France

Corresponding author: Robert.wojcieszak@univ-lille.fr

Table of Contents figure

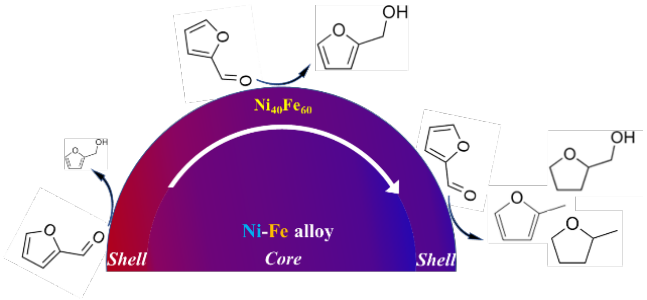

ABSTRACT

Nickel is known for its high activity in the hydroconversion of furfural, and also for its poor selectivity to furfuryl alcohol as it also catalyzes the hydrogenolysis of the alcohol function and the hydrogenation of the furan ring. Bimetallic Ni-Fe catalysts have been proposed in the literature as more selective systems. However, the rationalization of their performance lies on questions that have remained open so far, about the homogeneity of the Ni and Fe distribution within the nanoparticles and at their surface, and the reversibility of these distributions upon switching between oxidative and reductive atmospheres, a key issue for base metals alloys. To provide answers to these questions, a series of Ni-Fe/SiO_2 catalysts differing by their Ni and Fe molar proportions was prepared by deposition-precipitation and tested in the liquid-phase hydrogenation of furfural in isopropanol. By applying to these catalysts a combination of element-specific and surface-specific characterization techniques (^{57}Fe Mössbauer spectroscopy, X-ray absorption spectroscopy, LEIS), we have evidenced that, far from presenting a homogeneous chemical order, the reduced Ni-Fe nanoparticles exhibit a gradient of Ni concentration from a Ni-enriched core to Ni-depleted, Fe-enriched outer shells. These outer shells readily oxidize upon exposure to oxygen, but their former state is restored upon re-activation in H_2 at 400 °C. Across the tested composition range, an overall Ni proportion of 60 – 75 Ni at%, associated to a surface proportion of 35 – 45 Ni at%, provided the highest yield of furfuryl alcohol. Both the rate of hydrogenation of the aldehyde function and the rate of the competing secondary processes (hydrogenolysis, ring hydrogenation) increased upon increasing the surface Ni proportion, with the latter gaining prominence on Ni-rich surfaces. These results point to the need for Ni domains of limited size, located among a large proportion of Fe atoms, to restrict the hydroconversion process to its first stage, rather than to very active sites specific to the most selective catalysts, or to nominal compositions that would appear as particularly selective *per se*.

KEYWORDS: bimetallic catalysts, core-shell structure, furfural, furfuryl alcohol, selectivity, LEIS

1. INTRODUCTION

Furfural (FF) is a furanic aldehyde produced industrially since the 1930s by the dehydration of xylose, a pentose present in hemicellulose.[1–4] Several molecules of interest can be derived from FF through successive or parallel reactions with hydrogen. Furfuryl alcohol (FFA), obtained by the hydrogenation of the aldehyde function of FF, is an intermediate in the production of fine chemicals, fibers and rubbers. Secondary and tertiary products of hydroconversion, such as 2-methyl-furan (MF), tetrahydrofurfuryl alcohol (THFFA) and 2-methyltetrahydrofuran (MTHF) are used as solvents, fuel additives or chemical intermediates, and are obtained by hydrogenolysis or/and hydrogenation of the furan ring of FFA.[5–7] The selectivity of the catalyst employed in the hydroconversion of FF is thus of paramount importance if one of these products is targeted in particular. Restricting the transformation of FF to FFA requires a catalyst on which over-hydrogenation and hydrogenolysis reactions are avoided.

Noble metals have been largely employed for the liquid-phase hydroconversion of biosourced molecules but they are costly, and their abundance is low.[8–13] Ideally, substitutes should be found among the more abundant and cheaper first-row transition metals. While cobalt- and copper-based systems have been tested as selective to FFA, but with issues of stability and deactivation,[2,4] nickel, in contrast, is known both for its high activity and its poor selectivity, as it catalyzes the hydrogenation of both oxygenated functions and aromatic rings, hydrodeoxygenation reactions, and decarbonylation reactions.[14–22] However, tuning the catalytic performance of Ni can be done by association with a second metal within bimetallic nanoparticles. In recent years, Fe has been shown to be a promising and cost-effective candidate for the preparation of selective Ni-based systems. A $Ni_{75}Fe_{25}/Al_2O_3$ catalyst prepared by Putro et al. (where the two figures correspond to the molar proportions of the metals in the catalyst) provided a 92 % yield of FFA in isopropanol

at 150 °C, while the fully hydrogenated molecule, THFFA, was the main product formed with Ni/Al_2O_3 (selectivity: 61 %).[14] This tendency was confirmed by Shi et al. in similar conditions, using a $Ni_{62}Fe_{38}/SiO_2$ catalyst.[23] A high yield of FFA was also obtained in ethanol by Chieffi et al. using $Ni_{58}Fe_{42}/C$ (conversion of FF: 99 %; selectivity to FFA: 90 %),[24] and more generally in protic solvents by Jia et al., using a $Ni_{75}Fe_{25}/SiO_2$ catalyst (conversion of FF in methanol > 99 %; selectivity to FFA: 97 %).[25] Addition of water to methanol would lead to cyclopentanone by ring rearrangement.[26] These results in the liquid phase parallel the reported selectivity to FFA of Ni-Fe catalysts used in the vapor-phase conversion of FF,[27,28] and their selectivity to 2,5-furandimethanol in the hydrogenation of 5-hydroxymethylfurfural in butanol.[24] It can be noted that the current literature has mostly focused on a narrow range of Ni-Fe nominal formulations, roughly between $Ni_{60}Fe_{40}$ and $Ni_{80}Fe_{20}$, leaving open the question of the behavior of Fe-richer or Ni-richer systems.

Understanding the catalytic performance of Ni-Fe nanoparticles as a function of their formulation requires one to understand what lies at their surface. The Ni and Fe distribution at the surface of the Ni-Fe nanoparticles has been assumed to influence their hydroconversion properties.[29] Oxophilic Fe has been suggested to favor the adsorption of oxygenated functions, while DFT calculations and experimental measurements tend to indicate that alloyed or Fe-rich domains hinder the adsorption of aromatic rings compared with Ni.[14,16,20,30–33]

However, three aspects must be taken into account if one wants to draw firm correlations between the catalytic properties of Ni-Fe catalysts and the composition of the nanoparticles, and determine if the nominal composition of the catalyst is the relevant parameter to rationalize the catalytic performance. First, in order to avoid issues linked to structure-sensitivity and to the existence of a diversity of active sites, the Ni-Fe nanoparticles must exhibit similar size and composition throughout the catalyst, which is difficult to attain with standard preparation methods

such as incipient wetness impregnation,[34–36] but can be achieved using deposition-precipitation.[23,37] Second, it must be checked if the two metals are alloyed in a homogeneous manner inside the particles, core and outer shells alike, or if they are segregated. Reports of heterogeneous distributions of the metals within a given Ni-Fe nanoparticle can be found in the literature [20,38]. Last, both Ni and Fe being base metals prone to oxidation, the question is raised of the reversibility of metal dealloying or re-alloying when switching between an oxidizing environment, such as exposure to air, and a reducing environment, such as the initial reduction or re-activation in H_2. Dealloying was for example evidenced by X-ray absorption spectroscopy for Ni-Fe nanoparticles used for the dry reforming of methane.[39] Answering these questions requires not only characterization methods at the nanometer scale, but also their implementation in *in situ* conditions.

The objective of this work is to link the activity and selectivity of Ni-Fe catalysts in the liquid-phase hydrogenation of furfural, to the distribution of the two elements within and at the surface of the bimetallic nanoparticles. This distribution will be evaluated for a series of Ni-Fe/SiO_2 catalysts exhibiting different molar proportions of the two metals, along the various stages existing between the initial reduction of the catalyst in hydrogen and the catalytic test. A set of complementary characterization techniques will selectively inform on each element (X-ray absorption spectroscopy, ^{57}Fe Mössbauer spectroscopy), provide access to atomic-resolution analysis (high-resolution transmission electron microscopy, coupled with high-resolution electron energy loss spectroscopy), and probe the outer shells of the nanoparticles (low energy ion scattering spectroscopy). In this way, it will be determined to what extent the bulk composition of the nanoparticles is reflected in their surface composition, if reversible or irreversible changes

occur during the catalyst's life, and how the surface characteristics of the Ni-Fe nanoparticles condition their selectivity toward FFA or to other reaction products.

2. EXPERIMENTAL SECTION

2.1. Catalysts preparation

Six Ni-Fe/SiO_2 catalysts differing by the proportions of the metals, and a reference Ni/SiO_2 catalyst, were prepared using a procedure of deposition-precipitation with urea (DPU) on silica described in detail elsewhere.[23] Nickel (II) and iron (II) sulfates (Aldrich, 99 % and Alfa Aesar, 98 %, respectively) were used as precursor salts, and Sipernat-50 silica as support (Degussa; surface area, 400 $m^2\ g^{-1}$, pore volume, 1.4 $cm^3\ g^{-1}$). The total Ni+Fe concentration in the DPU solution was constant for the seven syntheses (0.28 mol L^{-1}). The molar proportions of Ni and Fe in solution are presented in **Table 1** for each preparation. The initial DPU suspension containing silica, sulfuric acid (Alfa Aesar, 93 – 98 %), urea (Alfa Aesar, 99 – 100 %) and nickel sulfate was degassed with Ar before introduction of iron sulfate, and heated to 80 °C. An atmosphere of Ar was maintained during the 22 h of deposition-precipitation, in order to avoid the oxidation of Fe^{2+} to Fe^{3+} and the separate precipitation of iron (III) compounds. After filtration and drying at room temperature under Ar, storage took place in air, which resulted in the quantitative oxidation of Fe^{2+} to Fe^{3+} as verified by Mössbauer spectroscopy (**Figure S1**). In all cases, powder X-ray diffraction (diffraction peaks at 2θ = 8.17, 16.39 and 24.69°) and ^{57}Fe Mössbauer spectroscopy applied to the dried solids confirmed the formation of poorly organized 1:1 phyllosilicates containing Fe^{3+}. The association between Fe^{3+} and Ni^{2+} ions in the mixed phyllosilicates was evidenced via the linear decrease of the average quadrupole shift of Fe^{3+} when the Ni fraction increased, which would not occur if Fe^{3+} was present in segregated ferric phases only (**Table S1**).

The preparation of the catalysts ended with a reduction step of the dried solids in a flow of 10 % H_2/Ar (100 mL min^{-1}) at 5 °C min^{-1} up to 700 °C with a plateau of 2 h, without preliminary calcination. This temperature was chosen in order to ensure the reduction of Fe to the metallic state.[23]

Elemental analysis was performed by X-ray fluorescence (XRF) for the determination of the metals contents in reduced catalysts. Molar proportions were corroborated by ICP-OES measurements on the dried solids. On the basis of the dispersion of measurements for individual XRF scans, absolute errors were conservatively estimated to be ± 4 %. The total metal loadings and molar proportions of Ni and Fe (calculated as Ni/(Ni+Fe) and Fe/(Ni+Fe)) are presented in **Table 1**. Catalysts will be denoted using these measured molar proportions: $Ni_xFe_{(100-x)}/SiO_2$. Except for $Ni_{35}Fe_{65}/SiO_2$, whose total metal content is significantly larger than that of the next ones in the series, metal loadings were found to increase in the 49 – 59 wt% range when the Ni molar proportion increased. As was observed before,[23] nickel was deposited preferentially with respect to iron during the DPU process: the nickel molar proportion on the catalyst was almost always larger than that of the corresponding DPU solution. Nevertheless, the Ni proportion in the solids increased monotonically when the Ni fraction in the DPU solution increased, and the result is a series of Ni-Fe catalysts that displays an increasing proportion of nickel and, conversely, a decreasing proportion of iron.

2.2. Characterization

Powder X-ray diffraction patterns (XRD) were recorded in ambient conditions using the Cu Kα radiation (λ = 1.5418 Å; 40 kV, 30 mA) on a Siemens D5000 diffractometer, with a 0.05° scan step and 2 s time step. X-ray fluorescence spectroscopy (XRF; M4 Tornado, Bruker) was used to

estimate the elemental composition of the reduced catalysts. To obtain accurate quantification of the metals loading in the catalysts, each sample was irradiated 30 times. Fe and Ni elemental analysis was also performed on dried solids by inductively coupled plasma-optic emission spectroscopy, using a 720-ES ICP-OES spectrometer (Agilent) with axial viewing and simultaneous CCD detection. N_2 physisorption isotherms at liquid nitrogen temperature were carried out on a TriStar II Plus gas adsorption analyzer (Micromeritics) after activation at 150 °C in vacuum overnight. The specific surface area was evaluated with the Brunauer-Emmett-Teller (BET) model over the range $P/P_0 = 0.05 – 0.30$. Temperature-programmed reduction (TPR) was followed using an Autochem apparatus (Micromeritics) under H_2 (5 %)/Ar (flow rate: 50 mL min^{-1}; ramp rate: 7.5 °C min^{-1}).

^{57}Fe Mössbauer spectra were measured with a source of ^{57}Co embedded in a rhodium metal matrix. Measurements were performed in the transmission mode, with the source at room temperature. The measured sample, in the form of powder, was mounted in a gas flow reactor working at controlled temperatures up to 700 °C under diluted H_2 (5 %)/Ar flow (flow rate: 50 mL min^{-1}). The sample was then transferred into an appropriate airtight sample holder within an Ar-filled glove box (O_2, H_2O < 1 ppm) to avoid exposure to ambient air, and to a helium gas flow cryostat for measurement at −268 °C (5 K). For two catalysts (section 3.4), the airtight holder was then opened for exposure to ambient air. The sample was recovered, remounted in the gas flow reactor and re-activated at 400 °C under diluted H_2 flow, before measuring a Mössbauer spectrum at 5 K as described above, strictly avoiding any contact with ambient air. The spectrometer was operated with a triangular velocity waveform, and a gas-filled proportional counter was used for the detection of the gamma rays. Velocity calibration was performed with an α-Fe foil. The isomer shift δ, the electric quadrupole splitting Δ, the magnetic hyperfine field B_{HF}, the linewidth at half

maximum Γ and the relative absorption area of the different components were determined by fitting the spectra to appropriate combinations of Lorentzian profiles. The isomer shifts are given relative to α-Fe at room temperature.

Electron microscopy was carried out on the microscopy facility of the Advanced Characterization Platform of the Chevreul Institute, Lille. Bright-field TEM images for the determination of size histograms were obtained using a Tecnai G2 20 microscope equipped with a LaB_6 filament and operating at 200 kV. For the analysis of individual nanoparticles, high resolution Scanning Transmission Electron Microscopy (STEM) was performed on a TITAN Themis 300 S/TEM microscope equipped with: a probe aberration corrector and monochromator, allowing spatial resolution of 70 pm and energy resolution of 150 meV; a super-X windowless 4 quadrant SDD (silicon drift detector) detection system for STEM-EDX mapping and several annual dark field detectors; a high resolution post-column GIF, the GATAN's Quantum ERS/966 with 2kx2k Ultrascan camera with 994G sensor, for the acquisition of electron energy loss spectra. In order to investigate the elemental distribution within bimetallic particles, high-angle annular dark field (HAADF) imaging and high-resolution electron energy loss spectroscopy (HR-EELS) were carried out in the STEM mode. Measurements were performed with a spot size of about 500 pm, a semi-convergence angle between 16 and 21 mrad, and a probe current of approximately 100 pA. For HAADF images, collection angles were chosen between 50 and 200 mrad. Dual EELS acquisition was performed in the spectral imaging mode with a collection angle of 49 mrad, a dispersion of 0.25 eV/ch, a step between 150 and 700 pm, and a dwell time between 50 and 200 ms. Alignment of the energy drift was done on the zero-loss peak. When possible, noise reduction by PCA was performed on the spectrum images using HyperSpy.

Time-resolved X-ray absorption spectroscopy (XAS) data were obtained in the transmission mode at the ROCK beamline (synchrotron SOLEIL), using the home-made Quick-EXAFS monochromator equipped with a Si (111) channel-cut crystal.[40,41] The channel-cut oscillates with a ± 1.95° amplitude around 14.6° and with a frequency of 2 Hz, allowing simultaneous recording of the Fe (7112 eV) and Ni (8333 eV) K-edge spectra in 250 ms. Successive spectra collected with upward Bragg angles during the *in situ* monitoring of catalysts were merged to improve the signal-to-noise ratio, leading to a time resolution of 5 s per spectrum effectively analyzed. Ionization chambers provided by Ohyo Koken Kogyo Co. Ltd. filled with a 2:1 mixture of N_2 and He were used for measurements. The beam size was 2.5 x 0.5 mm. The *in situ* re-activation of reduced catalysts formerly exposed to ambient air was performed by heating the Lytle-type cell containing the sample from room temperature to 500 °C under a H_2 (5 %)/He flow (50 mL min^{-1}) with a heating rate of 5 °C min^{-1}. The oxidation of two reduced catalysts was performed at 80 °C under a O_2 (10 %)/He flow (35 mL min^{-1}) after a purge under N_2 (30 mL min^{-1}). Normalization of spectra was performed by using the Python normal_gui graphical interface developed at SOLEIL for the fast handling of Quick-XAS data.[42] The proportions of the different Fe and Ni species were determined by a multivariate data analysis, the MCR-ALS method.[43-45][42–44] MCR-ALS GUI 2.0 developed by the Tauler group,[46][45] and freely available as a Matlab toolbox, was used for MCR-ALS analysis. The EXAFS signal extraction and Fourier transform of the EXAFS spectra were done using the Athena graphical interface software.[47][46] EXAFS fitting of interatomic distances, coordination numbers and Debye-Waller factors was performed with the Artemis interface to IFeFFIT using least-squares refinements,[48][47] firstly checked on NiO, Ni metallic foil and Fe_2O_3 references. Fourier-transformed EXAFS signals are presented without phase correction.

The low-energy ion scattering (LEIS) analyses were performed on a Qtac100 spectrometer (IONTOF GmbH) following a protocol described in a former report.[4948] A 5 keV Ne^+ beam at normal incidence was selected for quantitative Fe and Ni analysis (1 nA beam current).[5049] Prior to LEIS measurements, the samples formerly reduced at 700 °C and exposed to air were re-activated *in situ* under pure hydrogen at 400 °C for 2 h in a dedicated cell coupled to the spectrometer, allowing transfer under ultra-high vacuum without air contamination. The ionic dose per spectrum was first limited to 0.05 x 10^{15} ions cm^{-2} for the first ten spectra (theoretically corresponding each to 5 % of a monolayer of a flat surface assumed to exhibit 10^{15} atoms cm^{-2}), then was increased to 1.2 × 10^{15} ions cm^{-2} in order to complete the analysis of the surface and analyze the composition of the sub-surface. The data were processed using the SurfaceLab software from the same manufacturer. The LEIS signal was decomposed using the experimental lineshapes provided by the Fe and Ni peaks of the Fe_2O_3 and NiO reference materials (at 1202 and 1289 eV, respectively) in order to take the isotopic distribution of each metal into account. In the measurements presented in section 3.5, the Fe peak was found at 1210 ± 10 eV, and the Ni peak at 1290 ± 10 eV; these intervals come from differences of charge compensation. The ratio of the sensitivity factors η(Fe) / η(Ni) used for the relative quantification of the two metals was previously determined to be equal to 0.89.[4948]

2.3. Catalytic tests

The hydrogenation of furfural was tested using a Screening Pressure Reactor (SPR) system from Unchained Labs equipped with 24 parallel stainless-steel batch reactors of 6 mL each. Tests were performed at 150 °C under 20 bar H_2 and a continuous agitation of 600 rpm for all the tests (orbital shaking). Catalysts formerly reduced at 700 °C and stored in air were weighed, introduced

into the reactors, and re-activated *in situ* at 400 °C in pure H_2 for 2 h (400 °C being the highest temperature that can be attained in the set-up). 1.5 mL of FF solution in isopropanol was then added into each reactor inside a glove-box, in order to avoid the re-oxidation of the catalysts. All the solutions tested by GC after reaction were filtered to eliminate the catalyst. Reaction products were analyzed using a Shimadzu GC-2010 Plus gas chromatograph, equipped with a FID detector, a ZB-5MS column (30 m x 0.25 mm x 0.25 µm).

The amount of furfural was fixed at 0.56 mmol (concentration: 0.37 mol L^{-1}), in order to minimize the amounts of ethers formed between the alcohols resulting from the hydroconversion of FF and the isopropanol solvent.[23] A mass of 10 mg of catalyst was first used for different reaction times, 1, 2 and 4 h. However, it was found that for the most active catalysts, conversion already reached 100 % for the shortest reaction time, which did not allow comparison with the less active systems, or estimation of an initial reaction rate. A significant decrease of the conversion could only be achieved by decreasing both the reaction time and the catalyst mass at the same time, while staying in satisfactory accuracy domains. The following couples of parameters were thus used: 0.5 h, 3 mg; 0.5 h, 5 mg; 1 h, 3 mg; 1 h, 5 mg. As a consequence, the catalysis figures will be plotted as a function of the product between reaction time and the mass of catalyst, namely: 1.5 (0.5 h * 3 mg), 2.5 (0.5 h * 5 mg), 5 (1 h * 5 mg), 10 (1 h * 10 mg), 20 (2 h * 10 mg) and 40 h * mg (4 h * 10 mg). As selectivities cannot be compared at identical conversion across the whole catalysts series, given the very different catalytic performance, furfural consumption and yields of products will be compared, using mmol as unit. The slope of the curves will thus correspond to reaction rates expressed in mmol of FF consumed per mg of catalyst and per hour (mmol mg_{cat}^{-1} h^{-1}), which will be further normalized per m^2 of exposed metal.

Recycling tests were carried out in a 30 mL batch Hastelloy Parr reactor, so that a larger amount of catalyst could be used and recovered. 24 mL of furfural solution in isopropanol (0.38 mol L^{-1}) and 174 mg of catalyst were loaded into the reactor. Compared with the SPR experiments involving 10 mg of catalyst, the increase of the catalyst mass was proportional to the increase of solution volume and related furfural amount. Re-activation at 400 °C under H_2 was performed before each test using the SPR set-up, and the catalyst was transferred to the Parr reactor under inert atmosphere. After purging the reactor 3 times with H_2, 20 bar H_2 was added, the reaction temperature was set to 150 °C and the stirring rate to 600 rpm (mechanical stirring). At the end of the reaction, the H_2 pressure was removed, the reactor was cooled, the catalyst was collected by centrifugation and dried overnight at 60 °C before being re-activated in H_2 for the next test.

It was also verified with the Parr reactor, by attempting to convert furfural under N_2 pressure in the absence of H_2 for 2 h, that hydrogen transfer from isopropanol to furfural did not occur in these experimental conditions either using the $Ni_{62}Fe_{38}/SiO_2$ or the Ni_{100}/SiO_2 catalyst.

3. RESULTS AND DISCUSSION

3.1. Characterization of the Ni-Fe nanoparticles after reduction at 700 °C and exposure to air

All XRD patterns recorded in ambient conditions after reduction at 700 °C evidence three diffraction peaks at about 43 – 44, 50 – 51 and 74 – 75°, assigned to the (111), (200) and (220) reflections of *fcc* metallic phases, and close to the positions expected for *fcc* Ni (**Figure S2**). No metal segregation between particles of different structures (for example, *bcc* Fe-based particles) was evidenced. The diffraction peaks were shifted towards larger angles (*i.e.*, interplanar distances were smaller) when the Ni molar proportion increased, and the value of the unit cell parameter *a*,

calculated from the (200) reflection to avoid any possible interference with the NiO (200) peak at 43.4°, decreased (**Table S2**). This is in line with the slightly smaller atomic radius of Ni compared with that of Fe (0.124 *vs*. 0.126 nm) and indicates that the two metals are alloyed at least in the crystalline core of the nanoparticles. In a former work,[23] and in line with the literature,[5150] the unit cell parameter *a* of Ni-Fe alloys was shown to decrease linearly with the increasing Ni content. This Vegard's law was used for a rough assessment of the atomic proportions of Ni and Fe in the crystalline core of the particles. Analysis by XRD and XRF led to consistent results (**Table 1**). It should be noted that the values deduced from the Vegard's law inform on the average composition of the nanoparticles, but not on the possible existence of heterogeneities. The specific surface area of the reduced catalysts, calculated with the BET model, is also presented in **Table 1** and its evolution with the Ni proportion will be discussed in section 3.7.

Table 1. Proportions of Ni and Fe in the DPU solutions, and characteristics of the reduced catalysts: metal loading, molar proportions of Ni and Fe, specific surface area.

Samples	Proportions of Ni and Fe in DPU solutions		Metal loading and molar proportions of Ni and Fe after reduction at 700 °C					Specific surface area (m^2 g^{-1})
			XRF/ICP			XRD		
	Ni (%)	Fe (%)	Metal loading (Ni+Fe wt%)	Ni (%)	Fe (%)	Ni (%)	Fe (%)	
$Ni_{35}Fe_{65}/SiO_2$	25	75	63	35	65	35	65	136
$Ni_{55}Fe_{45}/SiO_2$	40	60	49	55	45	55	45	162
$Ni_{62}Fe_{38}/SiO_2$	50	50	49	62	38	63	37	238
$Ni_{73}Fe_{27}/SiO_2$	60	40	54	73	27	71	29	224
$Ni_{84}Fe_{16}/SiO_2$	75	25	55	84	16	84	16	178
$Ni_{92}Fe_{8}/SiO_2$	90	10	58	92	8	89	11	135
Ni_{100}/SiO_2	100	0	59	100	0	100	0	137

Bright field TEM was used to determine the particle size distribution (**Figure S3**). Narrow size distributions centered in the 4 – 7 nm range were found for all the catalysts. The values of the average particle size are consistent with those calculated from the XRD patterns using the Scherrer equation (5 – 6 nm) (**Table S3**). Because the adsorptive properties of the particles depend on their surface composition, and adsorption stoichiometries of usual probe molecules are not known for Ni-Fe surfaces, the fraction of surface atoms, or dispersion D (%), was evaluated from the size histograms rather than from chemisorption measurements. The formula 97.1/Ø (nm) formerly used for hemispherical nanoparticles of *fcc* Ni was applied to each class of diameter Ø from the histograms. Values of D ranged from 17 to 19 % (**Table S3**). The metal surface area exposed per gram of catalyst was evaluated between 62 to 73 $m^2\ g_{cat}^{-1}$, assuming that one Ni or Fe atom occupies 6.3 $Å^2$ (**Table S3**).[52,5351,52]

Individual Ni-Fe nanoparticles on catalysts $Ni_{55}Fe_{45}/SiO_2$, $Ni_{62}Fe_{38}/SiO_2$, $Ni_{73}Fe_{27}/SiO_2$ and $Ni_{84}Fe_{16}/SiO_2$ were studied by STEM-EELS coupled to HAADF imaging, to evidence heterogeneities within the nanoparticles (**Figure 1**). The choice of the catalysts was based on relevance with respect to their very different catalytic properties despite similar metal specific surface areas, and to the sensitivity of the technique. In all cases, Ni-Fe nanoparticles from catalysts exposed to air exhibited a core-shell structure. The composition of the Ni-Fe alloyed core matched the composition deduced from XRD, but a 0.5 to 1-nm thick oxidized shell (EELS measurements are given on **Figure S4** as an example) appeared as depleted of Ni by 10 to 40 %. On some images (both HAADF and EELS elemental maps; see for instance **Figures 1b1-2**), it can be seen that the Fe-rich shell developed in an asymmetrical way and not all around the particles.

The measured compositions of the core of different particles are given for each catalyst in **Table S4**. The standard deviation for Fe is found to be 7 at%, though it should be acknowledged that some statistical samples are small. But this value is consistent with the standard deviation of 8 at% presented in our previous work for a $Ni_{62}Fe_{38}/SiO_2$ catalyst, and calculated from EDX measurements with a larger sampling of particles.[23]

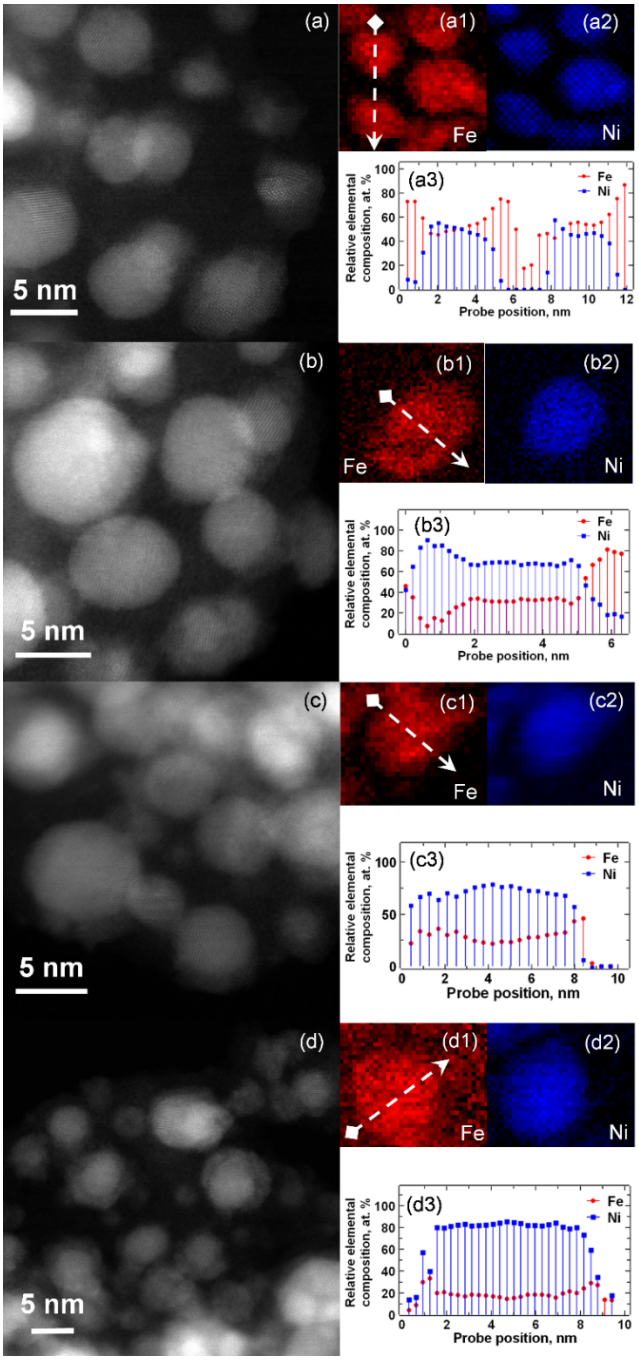

Figure 1. STEM - HAADF images and elemental maps for Fe-$L_{3,2}$ edge at 710.5 eV and Ni-$L_{3,2}$ edge at 856.5 eV, obtained by STEM - EELS mapping for $Ni_{55}Fe_{45}/SiO_2$ (a, a1-3), $Ni_{62}Fe_{38}/SiO_2$ (b, b1-3), $Ni_{73}Fe_{27}/SiO_2$ (c, c1-3) and $Ni_{84}Fe_{16}/SiO_2$ (d, d1-3) after reduction at 700 °C and exposure to air. Panels (a3-d3) show extracted concentration profiles for Fe (red, a1 – d1) and Ni (blue, a2 – d2), measured along the dashed arrow.

Despite the very different metal fractions, the DPU synthesis thus leads to Ni-Fe particles with similar crystal structure (alloyed *fcc* particles), similar narrow size distributions (low fraction of particles smaller than 3 nm or larger than 8 nm), similar metal dispersion, and, with respect to individual compositions, similar standard deviations (no monometallic particles, few particles with very large discrepancies in composition). After exposure to air, the bimetallic nanoparticles possess a Ni-Fe alloyed core and a Fe-enriched oxidized shell, in line with a former observation done by STEM-EDX in the literature.

3.2. Characterization of the Ni-Fe nanoparticles after reduction at 700 °C: *in situ* measurements under H_2

In situ Mössbauer spectroscopy was used to determine if this segregation of Fe toward the surface was already present prior to exposure to air, or if it was a consequence of it. Dried samples were reduced in H_2 at 700 °C and transferred to a gas-flow cryostat under protected atmosphere. Mössbauer spectra measured at 5 K on the four as-reduced samples investigated by STEM-HAADF are shown in **Figure 2**. All samples exhibited a dominant contribution from Fe(0) in a magnetic environment, exceeding in all cases 90 % of the total resonance area. Spectra were fitted with two sextets and slightly different hyperfine fields (blue curves). A decomposition into two

Fe(0) components was also reported in the literature for Mössbauer spectra recorded at room temperature on Ni-Fe nanoparticles supported on carbon.[38] It can be recalled here that this procedure does not necessarily imply the existence of two separate domains, but corresponds to a simplified way of dealing with the existence of gradients of concentrations in a continuum of environments inside the material (Supporting Information, p. S3). The isomer shifts were in the range typically observed for Fe(0) in Ni-Fe alloys,[5453] and the corresponding values of the hyperfine field B_{HF}, close to 29 – 30 and 33 T (**Table 2**), are characteristic of Ni-Fe alloys in which Ni or Fe is the major metal, respectively.[5554] In addition to these two components, a minor component accounting for about 10 % of the total resonance area was present at the centre of the spectrum, and can be attributed to traces of divalent or trivalent iron which were not totally reduced in the reactor (green curves), or to traces of reduced Fe(0) in non-magnetic environments (red curve).

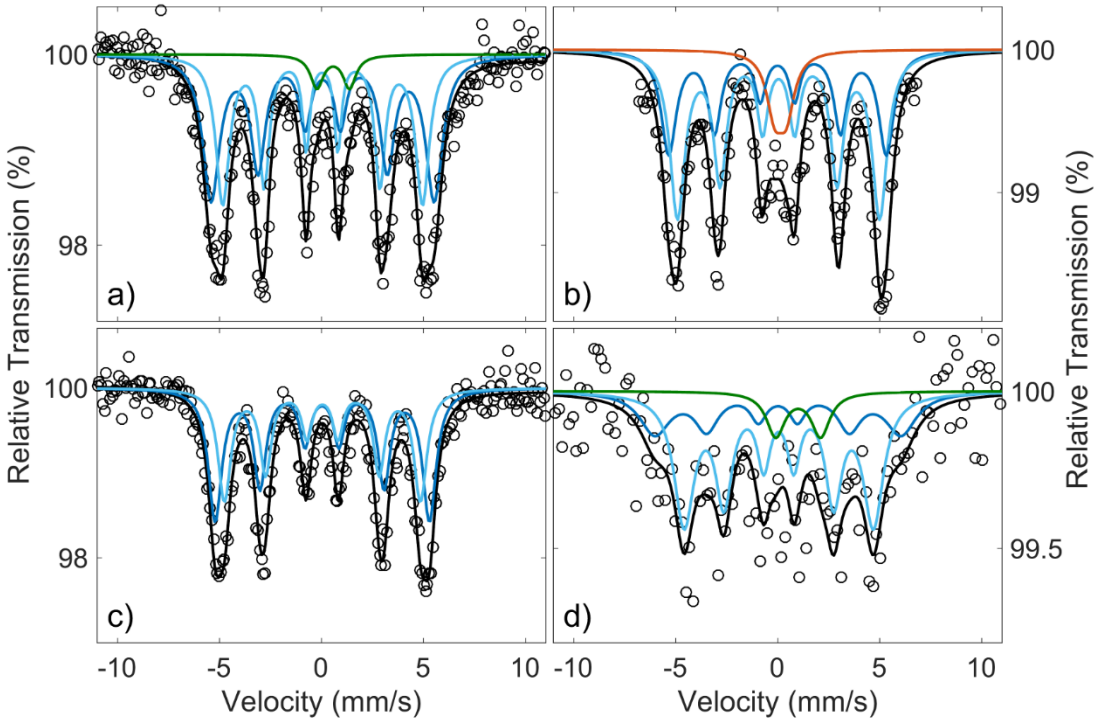

Figure 2. ^{57}Fe Mössbauer spectra measured at 5 K for samples $Ni_{55}Fe_{45}/SiO_2$ (a), $Ni_{62}Fe_{38}/SiO_2$ (b), $Ni_{73}Fe_{27}/SiO_2$ (c) and $Ni_{84}Fe_{16}/SiO_2$ (d), after reduction in H_2 flow at 700 °C.

Given the homogeneity in particle size and individual composition observed by TEM after exposure to air, the existence of different contributions for Fe(0) is consistent with an uneven distribution of Fe within the Ni-Fe particles, between a Ni-rich core (lower value of B_{HF}) and Fe-rich domains presumably in the outer shells (higher value of B_{HF}). It can also be seen that the lower value of B_{HF} decreases from 30.4 to 28.8 T (the value of B_{HF} expected for pure Ni) when the Ni proportion in the core of the particles increases, in agreement with XRD and TEM measurements. The enrichment in Fe when moving toward the surface thus predates the exposure to air and can be related to the late reduction of this metal compared with Ni.[23]

Table 2. ^{57}Fe Mössbauer hyperfine parameters at 5 K of samples $Ni_{55}Fe_{45}/SiO_2$, $Ni_{62}Fe_{38}/SiO_2$, $Ni_{73}Fe_{27}/SiO_2$ and $Ni_{84}Fe_{16}/SiO_2$, after reduction at 700 °C.

Samples	Site	δ (mm s^{-1})	Δ (mm s^{-1})	Γ (mm s^{-1})	Area (%)	B_{HF} (T)
$Ni_{55}Fe_{45}/SiO_2$	Fe(0), Ni-Fe core	0.15 ± 0.01	0	0.8 ± 0.1	44 ± 5	30.4 ± 0.2
	Fe(0), Ni-Fe surface	0.17 ± 0.02	0	1.0 ± 0.1	52 ± 5	33.9 ± 0.3
	Fe(II)	1.16 ± 0.08	1.6 ± 0.1	0.8 ± 0.1	4 ± 2	-
$Ni_{62}Fe_{38}/SiO_2$	Fe(0), Ni-Fe core	0.15 ± 0.02	0	0.9 ± 0.1	55 ± 8	29.8 ± 0.3
	Fe(0), Ni-Fe surface	0.10 ± 0.02	0	0.9 ± 0.1	35 ± 8	33.1 ± 0.4
	Fe(0), non magnetic	0.24 ± 0.04	0.6 ± 0.1	1.0 ± 0.1	10 ± 1	
$Ni_{73}Fe_{27}/SiO_2$	Fe(0), Ni-Fe core	0.1 ± 0.2	0	1.1 ± 0.1	63 ± 9	29.4 ± 0.2
	Fe(0), Ni-Fe surface	0.2 ± 0.2	0	0.8 ± 0.1	37 ± 9	33.6 ± 0.9
$Ni_{84}Fe_{16}/SiO_2$	Fe(0), Ni-Fe core	0.16 ± 0.04	0	1.2 ± 0.1	61 ± 7	28.8 ± 0.5
	Fe(0), Ni-Fe surface	0.1 ± 0.2	0	1.8 ± 0.2	29 ± 7	36 ± 2
	Fe(II)	1.2 ± 0.1	2.2 ± 0.1	1.1 ± 0.1	10 ± 3	-

δ: isomer shift; Δ: electric quadrupole splitting; Γ: line width at half maximum; B_{HF}: magnetic hyperfine field.

3.3. Evolution of the reduced Ni-Fe nanoparticles upon exposure to an oxidizing atmosphere

In order to get some insight into the process of oxidation of reduced Ni-Fe nanoparticles, the oxidation of reduced samples $Ni_{62}Fe_{38}/SiO_2$ and $Ni_{84}Fe_{16}/SiO_2$ was followed by Quick-X-ray absorption spectroscopy at 80 °C, a temperature chosen to allow a better thermal control (**Figure S5**). Recording of the spectra started while the catalysts reduced *in situ* were still kept in an H_2 atmosphere, making it possible to identify the very moment when oxidation would start. After a purge in N_2, the catalysts were exposed to diluted O_2. Summation over 10 spectra was performed to reduce the noise, and the gap between two points on **Figure S5a** corresponds to a time difference of 5 seconds. The kinetics of oxidation was extracted using a MCR-ALS analysis procedure restricted to the XANES region. Two components arose from the chemometrics analysis, one corresponding exactly to the initial, reduced metals, the other one to the oxidized elements (Ni^{2+} and Fe^{3+}, respectively, by comparison with the XANES spectra of NiO and Fe_2O_3; **Figure S5b**). For the two catalysts, oxidation took place in two stages. The very rapid first stage converted 20 % of Ni and 30 – 40 % of Fe to the oxidic form within the first 25 seconds. Oxidation would then proceed more progressively, without reaching an asymptotic value during the 30 min that the measurements lasted. It can thus be anticipated that storage in ambient air would also end with a slow and progressive oxidation of the nanoparticles, the proportion of oxidic phases in a given sample depending on the duration of the storage period.

3.4. Characterization of the Ni-Fe nanoparticles upon and after re-activation under H_2

Before catalytic test, the Ni-Fe/SiO_2 catalysts stored in air must be re-activated under H_2 in order to restore their metallic character. The process of reduction of the oxidized fractions was

first explored by temperature-programed reduction experiments followed by Quick-XAS (**Figures 3** and **S6**). Spectra were recorded at the Ni and Fe K-edges, in *in situ* conditions during a ramp in H_2 up to 500 °C. A quantitative analysis was carried out using the MCR-ALS procedure. In order to better extract the oxidized components from the mixture of oxidic and reduced species, each catalyst was calcined in air in a muffle oven at 200 °C for 10 h, and the spectrum from fully oxidized Ni or Fe, recorded *ex situ*, was added to the MCR-ALS matrix. The initial proportion of metallic Fe was also determined by a preliminary MCR-ALS analysis carried out on a matrix of initial spectra. The inclusion of the EXAFS region in the MCR-ALS procedure did not lead to the identification of oxides with precisely known structures, suggesting the existence of poorly defined Ni^{2+} - Fe^{3+} mixed phases in the oxidic fraction, and the MCR-ALS analysis was applied only to the XANES region.

The MCR-ALS analysis at the Ni K edge yielded only two contributions, Ni^{2+} and metallic Ni. The MCR-ALS analysis at the Fe K edge yielded three contributions, assigned according to the position of the edge with respect to reference compounds: Fe^{3+} ions, transforming into intermediate Fe^{2+}, and finally metallic Fe. Initially, the fraction of oxidized Fe was found to be larger than the fraction of oxidized Ni, in line with the observations presented in sections 3.1 and 3.3. An example of evolution during the temperature ramp is given on **Figure 3** for catalyst $Ni_{35}Fe_{65}/SiO_2$ (the corresponding figures for four other catalysts are presented on **Figure S6**; measurements were not performed on $Ni_{92}Fe_8/SiO_2$ for sensitivity issues at the Fe K-edge). Fe^{3+} ions started to transform into Fe^{2+} ions at 120 °C. The reduction of the oxidized Ni fraction to metallic Ni took place in the 240 – 350 °C range. The reduction of Fe^{2+} to metallic Fe started at 295 °C. It was checked from the study of the other catalysts that the final stage of reduction for Fe levelled off when the fraction of metallic Ni exceeded 80 – 85 %. The activation process of Ni and

that of Fe were linked, and the reduction of Fe was governed by the proportion of Ni in the nanoparticles: it can be seen that the onset of the reduction of Fe^{3+} to Fe^{2+} ions shifts from 130 °C for $Ni_{35}Fe_{65}/SiO_2$ to 60 °C for $Ni_{84}Fe_{16}/SiO_2$. The larger the Ni molar proportion, the lower the temperature range for Ni reduction back to the metallic state, and the lower the temperature at which Fe reverted to its metallic state.

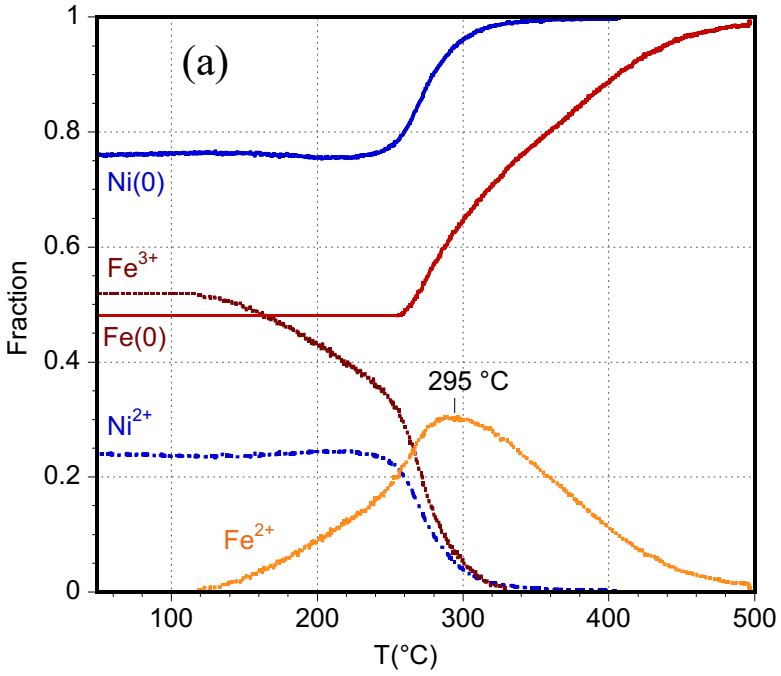

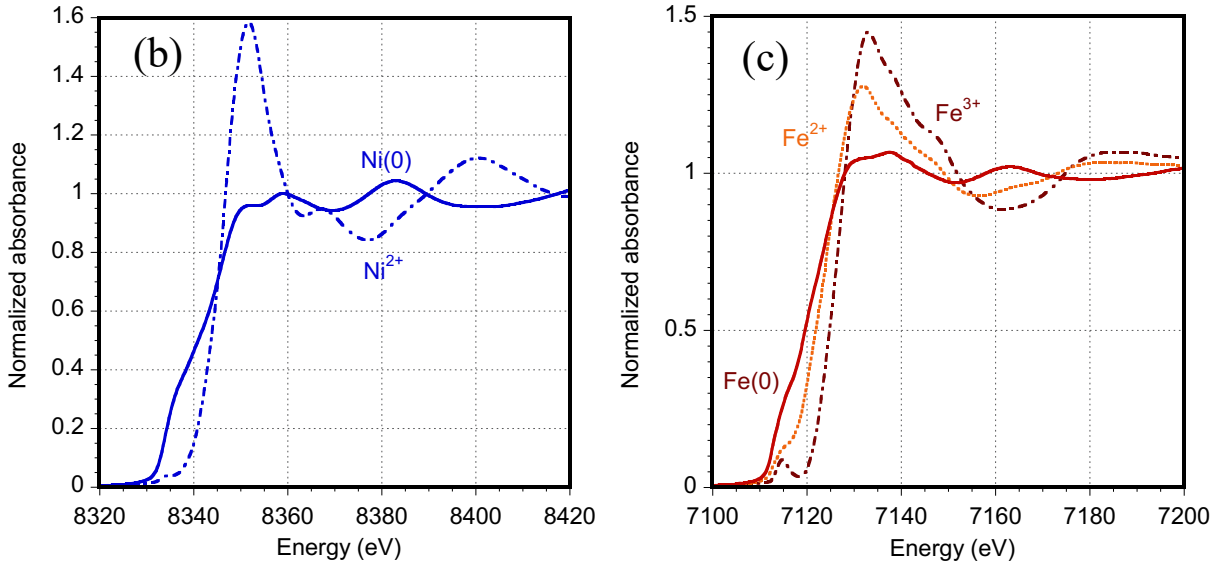

Figure 3. X-ray absorption spectroscopy: (a) concentration profiles obtained from MCR-ALS analysis of the activation under H_2 of $Ni_{35}Fe_{65}/SiO_2$; corresponding spectral components at the Ni K-edge (b) and Fe K-edge (c).

The structural characteristics of the re-activated nanoparticles, obtained by fitting the EXAFS oscillations and Fourier transforms at both the Ni and Fe K-edges for the first shell of neighboring atoms, correspond to the features described above. A detailed analysis can be found as Supporting Information (**Figures S7 and S8, Tables S5 to S8**). In brief, the four peaks observed on the Fourier transforms for the two metals, similar to those obtained for a Ni foil in terms of relative intensity and position, indicate that nickel and iron appeared predominantly in the metallic state, and in the *fcc* structure of the original bimetallic nanoparticles. At the Ni K-edge, the number of nearest neighbors was found to be higher than 10.7, which is consistent with the presence of Ni mostly in the core of the particles. The number of metallic neighbors around Fe was comprised between 8 and 9 and an oxygen contribution at a low distance had to be added. This discrepancy with respect

to Ni has been reported several times in the literature and attributed to the existence of Fe-enriched shells,[30,34,56-5855–57] a hypothesis strengthened by our own analysis of the nanoparticles composition. Both at the Ni and Fe K-edges, Ni-Fe interatomic distances R were found to consistently decrease upon increasing the Ni molar proportion, in line with the decrease of the cell parameter *a* determined by XRD. For each catalyst, the confidence intervals evaluated around R at the two edges overlapped and were in very good agreement.

Because temperature-programmed reduction is governed by kinetics, and re-activation in H_2 prior to catalytic test takes place at 400 °C only, the state of re-activated catalysts was also checked by applying Mössbauer spectroscopy to $Ni_{55}Fe_{45}/SiO_2$ and $Ni_{84}Fe_{16}/SiO_2$ after a series of three successive treatments: reduction in H_2 at 700 °C; exposure to air at room temperature; re-activation under H_2 at 400 °C. After re-activation, still under a H_2 atmosphere, temperature was decreased to 5 K and Mössbauer spectra were recorded. The hyperfine parameters and proportions of each contribution are presented in **Table S9**. They were globally unchanged with respect to the analysis performed after reduction at 700 °C (section 3.2). It was similarly verified by XAS that after the oxidizing treatment at 80 °C presented in section 3.3, the EXAFS Fourier transforms corresponding to metallic *fcc* Ni and Fe were recovered after a step of re-activation in H_2 at 400 °C.

In situ X-ray absorption and Mössbauer spectroscopies show that for catalysts exposed to air, the reduction of the Ni oxidized fraction to the metallic state drives the reduction of the oxidized Fe fraction (the higher the Ni content, the easier the reduction of Fe), and that the state of the nanoparticles after re-activation at 400 °C in H_2 is similar to that characterized after the initial reduction at 700 °C. Exposure of the catalysts to an oxidizing atmosphere thus does not induce an irreversible redistribution or dealloying of the metals.

3.5. Surface composition of Ni-Fe nanoparticles after re-activation under H_2

The techniques used above all suggest an enhanced Fe proportion in the outer shells, but do not probe these shells directly. In contrast, LEIS is based on the scattering of noble gas ions over the catalyst surface, and, after calibration on pure nickel and iron oxides (see Experimental section), gives access to a direct assessment of the distribution of Ni and Fe atoms lying at the extreme surface of the irradiated particles. As the surface is progressively etched by the ion beam, gradients of concentrations from the uppermost layers to the layers below can be evidenced.

LEIS measurements were applied to the six Ni-Fe/SiO_2 catalysts after reduction at 700 °C, exposure to air, and re-activation in H_2 at 400 °C. Transfer from the activation cell to the analysis chamber took place under ultra-high vacuum. The first recorded signals, at a very low ion dose, were poorly intense and corresponded to the removal of contamination (carbon, hydrogen…) by the ion beam; they were discarded for quantification. The intensity of the signal reached a maximum for a cumulative dose of 0.5 x 10^{15} Ne^+ ions cm^{-2}, which corresponded to the theoretical analysis of 50 % of a flat surface and was considered to reveal the atomic surface composition of the cleaned Ni-Fe nanoparticles. The cumulative ion dose was further increased to 7.8 × 10^{15} Ne^+ ions cm^{-2}, to progressively reveal the evolution of the composition in the outer shells, below the outermost layer. Given the lack of standardization for measurements on nanoparticles distributed over a porous support and the initial presence of contamination layers, translation of the results to a probed depth expressed in nm will not be attempted.

In order to exemplify the evolution of the composition along the Ni-Fe series, signals recorded for an identical dose of 4.1 x 10^{15} Ne^+ ions cm^{-2} are shown on **Figure 4**. The Ni molar proportion in the outer shells of the reduced Ni-Fe nanoparticles does increase when the global Ni proportion

increases in the catalyst, as can be seen from the increasing contribution of Ni to the LEIS signal (blue curves). But it is obvious that the Fe contribution dominates the signal for the first four catalysts, though only $Ni_{35}Fe_{65}/SiO_2$ contains more Fe than Ni in its nominal composition.

The profiles of the Ni molar proportion in the outer shells are shown as a function of the cumulative ion dose on **Figure S9**, and **Table 3** presents the values for cumulative ion doses of 0.5 x 10^{15} Ne^+ ions cm^{-2} (outermost probed layer), 7.8 x 10^{15} Ne^+ ions cm^{-2}, and in the middle of the range. In all cases, and in line with a measurement reported in the literature for a single catalyst,[5958] the surface of the reduced nanoparticles is very significantly enriched in Fe: the absolute depletion of Ni is in average 20 at% with respect to the nominal composition. On the other hand, the Ni molar proportion increases when moving deeper into the subsurface, which provides direct evidence for the existence of concentration gradients within the reduced nanoparticles, as suggested in the former sections. The increase of the Ni proportion is 10 at% in average across the probed depth, but the gradient is steeper for the catalysts with the higher proportion of Fe.

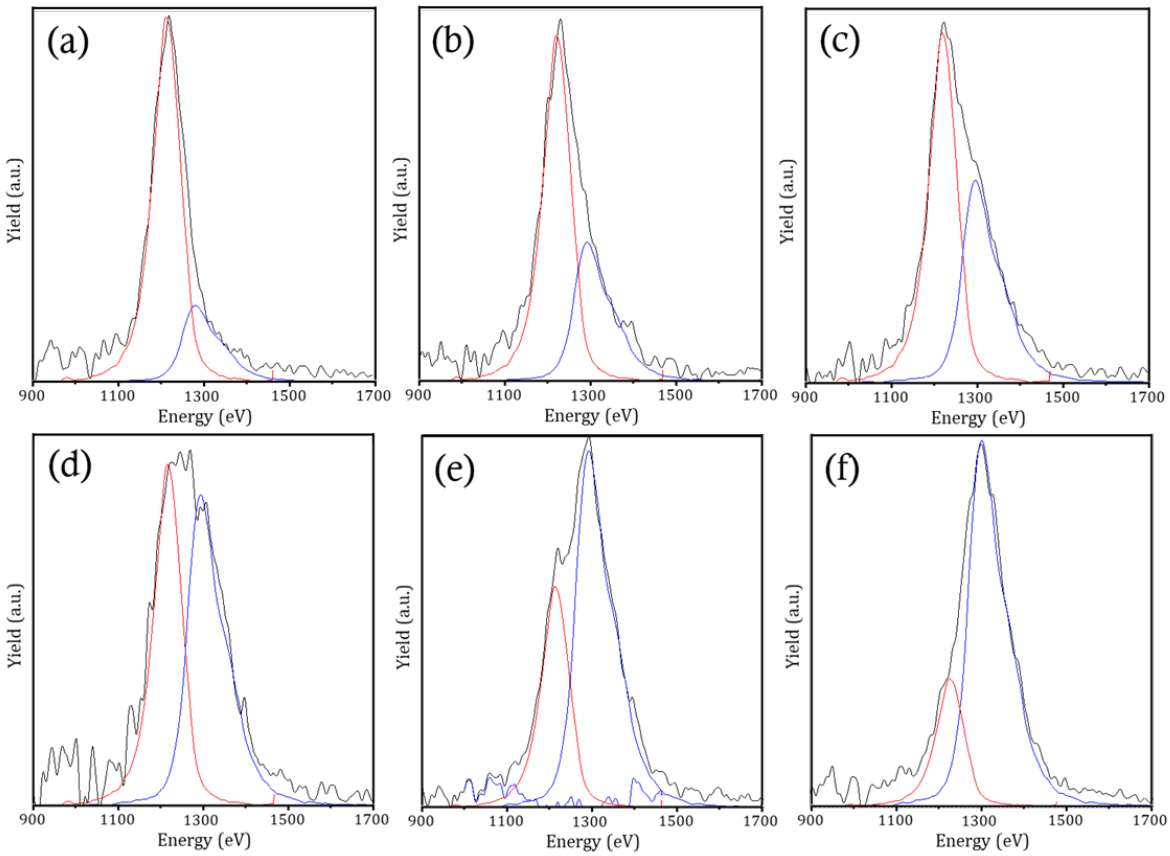

Figure 4. Decomposition of the LEIS spectra measured at a cumulative iso-dose of 4.1 x 10^{15} Ne^+ ions.cm^{-2} for catalysts $Ni_{35}Fe_{65}/SiO_2$ (a), $Ni_{55}Fe_{45}/SiO_2$ (b), $Ni_{62}Fe_{38}/SiO_2$ (c), $Ni_{73}Fe_{27}/SiO_2$ (d), $Ni_{84}Fe_{16}/SiO_2$ (e) and $Ni_{92}Fe_{8}/SiO_2$ (f). Red: Fe contribution; blue: Ni contribution.

In summary, LEIS measurements directly confirm the existence of a significant Fe enrichment and Ni depletion in the outer shells of the Ni-Fe reduced nanoparticles, and that of a concentration gradient when probing deeper inside the particles. The Ni atomic proportion in the outer shells still differs significantly from one catalyst to the other, making comparison in catalysis relevant. In the following, we will consider that the values reported in the first column of **Table 3** correspond to the composition of the outermost layer. Given that the analysis does not take place on a flat sample, and that it cannot be guaranteed that the etching of the surface of nanoparticles

supported on a porous oxide is done exactly layer by layer, we will conservatively add an absolute error bar, extending to the value reported for a cumulative dose of 4.1 x 10^{15} Ne^+.

Table 3. Atomic proportions of Ni and Fe deduced from LEIS measurements as a function of the cumulative dose of Ne^+ ions cm^{-2}.

Catalysts	0.5 x 10^{15} Ne^+	4.1 x 10^{15} Ne^+	7.8 x 10^{15} Ne^+
$Ni_{35}Fe_{65}/SiO_2$	$Ni_{13}Fe_{87}$	$Ni_{19}Fe_{81}$	$Ni_{23}Fe_{77}$
$Ni_{55}Fe_{45}/SiO_2$	$Ni_{21}Fe_{79}$	$Ni_{32}Fe_{68}$	$Ni_{39}Fe_{61}$
$Ni_{62}Fe_{38}/SiO_2$	$Ni_{37}Fe_{63}$	$Ni_{39}Fe_{61}$	$Ni_{45}Fe_{55}$
$Ni_{73}Fe_{27}/SiO_2$	$Ni_{46}Fe_{54}$	$Ni_{50}Fe_{50}$	$Ni_{55}Fe_{45}$
$Ni_{84}Fe_{16}/SiO_2$	$Ni_{64}Fe_{36}$	$Ni_{66}Fe_{34}$	$Ni_{69}Fe_{31}$
$Ni_{92}Fe_{8}/SiO_2$	$Ni_{75}Fe_{25}$	$Ni_{77}Fe_{23}$	$Ni_{76}Fe_{24}$

3.6. Catalytic performance of Ni-Fe/SiO_2 and Ni/SiO_2 catalysts

After analyzing the core and surface distributions of Ni and Fe in the nanoparticles, and ascertaining the reversibility of the changes taking places upon switches between oxidative and reducing atmospheres, the activity of the Ni-Fe catalysts was determined in the hydrogenation of furfural, compared with the monometallic Ni_{100}/SiO_2 catalyst, and correlated to their composition.

In line with the preliminary catalytic measurements formerly presented,[23] six reaction products were identified: the primary product, furfuryl alcohol, FFA; tetrahydrofurfuryl alcohol, THFFA; 2-methylfuran, MF; 2-methyltetrahydrofuran, MTHF; and two ethers identified by GC/MS, 2-(isopropoxymethyl)furan, iPrOMF, resulting from the etherification of FFA with the

isopropanol solvent, and 2-(isopropoxymethyl)tetrahydrofuran, iPrOMTHF, resulting from the etherification of THFFA with isopropanol. THFFA, MF and iPrOMF are secondary products resulting from the transformation of FFA by hydrogenation of the furan ring, hydrogenolysis and etherification reactions, respectively. MTHF and iPrOMTHF are tertiary products. The reaction scheme is shown on **Figure S10**.

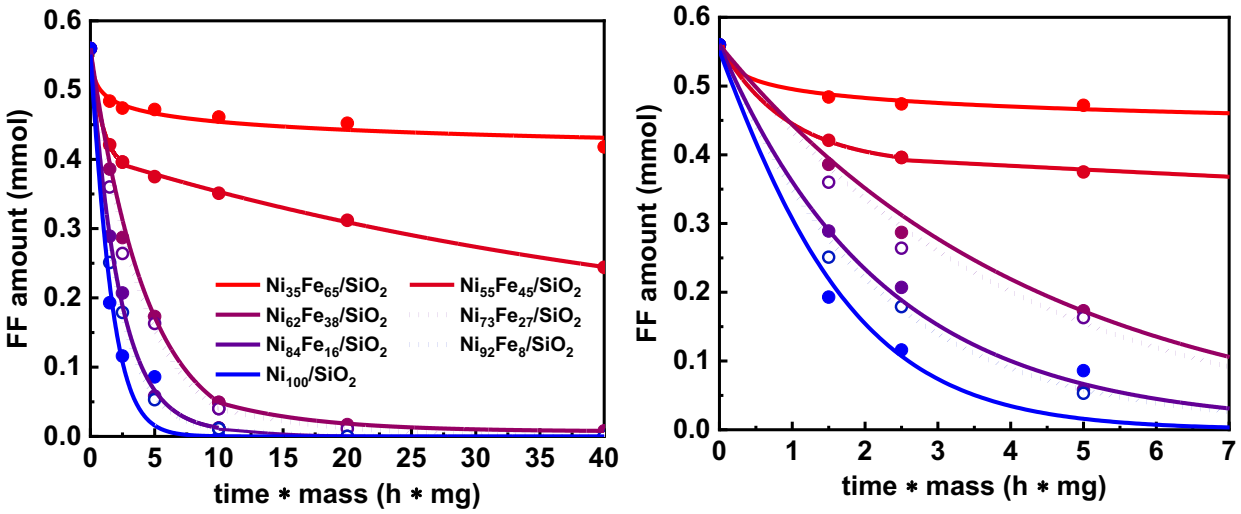

Figure 5. Furfural consumption for Ni-Fe/SiO_2 catalysts as a function of the (time * mass) product. Left: whole curves, right: zoom on the shorter time range. Reaction conditions: T = 150 °C, P(H_2) = 20 bar, solvent: isopropanol, volume of solution: 1.5 mL, $m_{catalyst}$ = 3 – 10 mg, t = 0.5 – 4 h.

The FF consumptions were first compared as a function of the (time * mass) product. As shown in **Figure 5**, FF was not fully consumed using the two catalysts exhibiting the lowest Ni proportions, $Ni_{35}Fe_{65}/SiO_2$ and $Ni_{55}Fe_{45}/SiO_2$, even after 4 h with 10 mg of catalyst. A full conversion was achieved when the Ni content increased further. The richer the Ni content of the catalyst, the higher the activity for the transformation of FF to FFA.

The carbon balance was evaluated as a function of the (time * mass) product (**Table S10**). Only for $Ni_{35}Fe_{65}/SiO_2$ and $Ni_{55}Fe_{45}/SiO_2$ were carbon balances slightly lower than 90 %. It can be hypothesized that because of the low conversion, the FF concentration remained high in the reaction medium, and resulted in its adsorption onto the surface of the catalysts. Products of degradation not detected by GC can also be responsible for the lower carbon balance. Carbon balances higher than 95 % were conversely achieved for Ni-richer catalysts.

The product yield was plotted for each catalyst as a function of (time * mass) (**Figure 6**). For $Ni_{35}Fe_{65}/SiO_2$, the main product was FFA, even though produced in a very low amount that did not change with time (0.02 mmol). This may support the existence of a deactivation process caused by the adsorption of FF or other derivatives on the active sites. Only after 4 h of reaction with 10 mg of catalyst, would the hydrogenolysis product, MF, appear, but only as traces. $Ni_{55}Fe_{45}/SiO_2$ was also selective to FFA, giving a higher yield. Other products, such as the ether iPrOMF, appeared at longer reaction times, but in very minor amounts.

A further increase of the Ni content (catalyst $Ni_{62}Fe_{38}/SiO_2$) led to a noticeably higher yield of FFA, making it the most selective catalyst in the series (0.45 mmol after 2 h of reaction with 10 mg of catalyst). However, FFA started to undergo secondary reactions when increasing the reaction time, mainly etherification to iPrOMF. In contrast, the amounts of THFFA and MF (maximum amounts: 0.025 mmol and 0.035 mmol) were similar to those measured for $Ni_{55}Fe_{45}/SiO_2$. MTHF remained a very minor product. The yields of FFA and, to a lesser extent, iPrOMF, measured for $Ni_{73}Fe_{27}/SiO_2$ were quite similar to those measured for $Ni_{62}Fe_{38}/SiO_2$, making $Ni_{73}Fe_{27}/SiO_2$ the second most selective catalyst of the series with respect to FFA. However, the amounts of secondary and tertiary products, THFFA, MF and MTHF, progressively

increased as a function of (time * mass), indicating that even a 10 at% increase of Ni in the catalyst could favour side-reactions.

A dramatic impact on the yield of FFA occurred for $Ni_{84}Fe_{16}/SiO_2$. FFA, that reached a yield of 0.335 mmol at its maximum, was now found to be rapidly consumed (above time * mass = 5 h mg), mainly by etherification to iPrOMF, that ultimately became the major product of reaction. The hydrogenolysis to MF and, to a lesser extent, the ring hydrogenation to THFFA, also gradually impacted the products slate, with final amounts of 0.089 and 0.081 mmol, respectively. The production of MTHF also increased, but this was not a major transformation pathway. The slight decrease of the production of MF, whereas the production of THFFA increased almost linearly with time without presenting a maximum, suggests that MTHF was mainly produced by the hydrogenation of the ring of MF.

The same tendencies were found for $Ni_{92}Fe_8/SiO_2$, with an even earlier consumption of FFA, and lower amounts of iPrOMF and MF. In this case, it was the production of THFFA, the fully hydrogenated molecule, that increased dramatically, as it became the predominant product along with iPrOMF. As a consequence, the ether associated to THFFA, iPrOMTHF, that could form either by etherification of THFFA, now present in a large amount, or by ring hydrogenation of iPrOMF, was detected. In line with the higher activity in the ring hydrogenation pathway, the amount of MTHF slightly increased compared with $Ni_{84}Fe_{16}/SiO_2$. Here also, its production could be correlated to the consumption of MF.

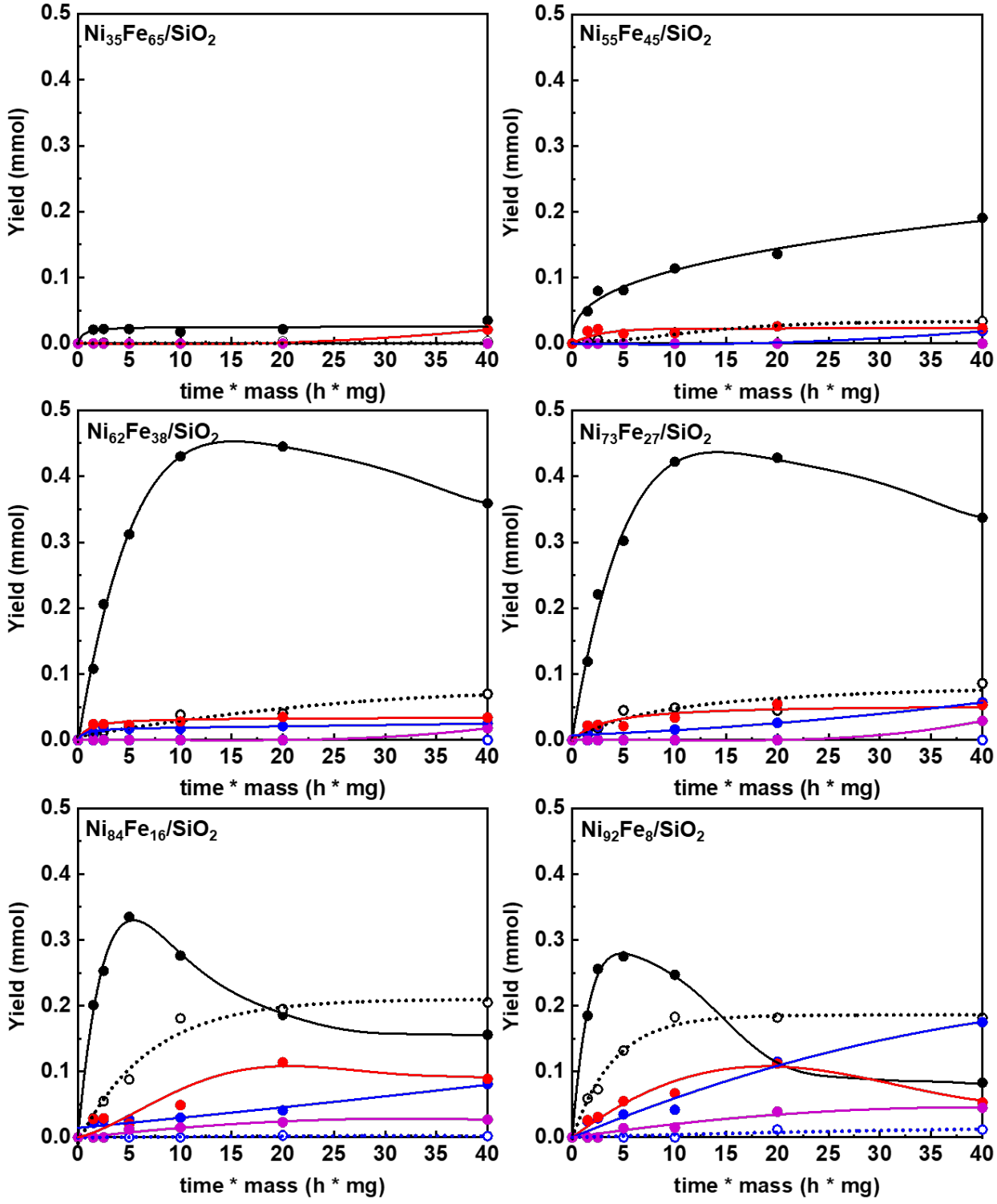
Ni35Fe65/SiO2
Ni55Fe45/SiO2
Ni62Fe38/SiO2
Ni73Fe27/SiO2
Ni84Fe16/SiO2
Ni92Fe8/SiO2
Yield (mmol)
time * mass (h * mg)
0.0
0.1
0.2
0.3
0.4
0.5
0
5
10
15
20
25
30
35
40

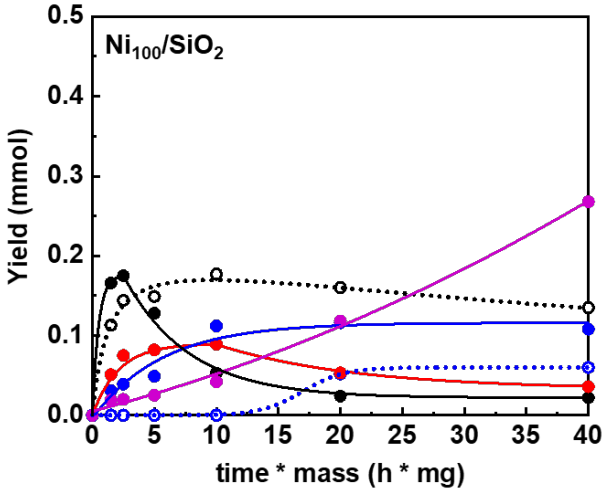

Figure 6. Yield of products as a function of (time * mass) for Ni-Fe/SiO_2 and Ni_{100}/SiO_2 catalysts. Black line (—●—): FFA; Black dotted line (···○···): iPrOMF; Blue line (—●—): THFFA; Blue dotted line (···○···): iPrOMTHF; Red line (—●—): MF; Purple line (—●—): MTHF. Reaction conditions: T = 150 °C, $P(H_2)$ = 20 bar, solvent: isopropanol, volume of solution: 1.5 mL, $m_{catalyst}$ = 3 – 10 mg, t = 0.5 – 4 h.

Finally, the trends found for monometallic Ni_{100}/SiO_2 consisted in an amplification of those identified for $Ni_{92}Fe_8/SiO_2$. FFA started to be consumed from (time * mass) = 2.5 h mg. The three secondary products appeared as early as the first measurement, in the following decreasing amount: iPrOMF, MF and THFFA. But both MF and iPrOMF were progressively consumed, and only the production of THFFA continued to increase till a plateau was reached. The associated ether, iPrOMTHF, appeared for (time * mass) = 20 h mg, via the etherification of THFFA or the ring hydrogenation of iPrOMF. Finally, the ring hydrogenation pathway led to a linear increase of the MTHF production, which became the major product. The presence of a clear maximum for the production of MF confirmed that MTHF was formed by hydrogenation of MF. However, the plateau reached for THFFA could also indicate that MTHF was partly formed via the

hydrogenolysis of THFFA. Overall, the Ni_{100}/SiO_2 catalyst was characterized by its high activity in both the ring hydrogenation and hydrogenolysis pathways, the former becoming predominant.

Selectivities obtained at full conversion for a mass of catalyst of 10 mg and a reaction time of 2 h are presented in **Table S11**, so as to better evidence the influence of the increasing Ni proportion on the catalytic performance.

Information about the recyclability of the $Ni_{62}Fe_{38}/SiO_2$ and Ni_{100}/SiO_2 catalysts is provided as Supporting Information (**Table S12**, **Figures S11 and S12**). It was verified in particular that the LEIS spectrum recorded on twice-recycled $Ni_{62}Fe_{38}/SiO_2$ did not change significantly compared with that from the catalyst just after re-activation and prior to reaction (**Figure S12**).

3.7. Discussion of the catalysis data

In order to get more insight into the nature of the active sites at the surface of the Ni-Fe nanoparticles, the initial rate of FF consumption - in other terms, the rate of hydrogenation of the aldehyde function - was calculated from the amount of FF remaining at (time * mass) = 1.5 h mg, and was normalized with respect to the exposed metal surface area in m^2. An error bar was calculated, based on a relative error of 5 % on the determination of the FF amount (repeatability of measurements), an absolute error of 4 % on the metal content, and an absolute error of 1 % on metal dispersion. The rate increased linearly with the Ni nominal molar proportion (**Figure 7a**). The intercept of this linear trend with axis x is located above 0, suggesting that the rate is not strictly proportional to the number of Ni atoms, and that a minimum amount of Ni is required to initiate the hydrogenation of the aldehyde function.

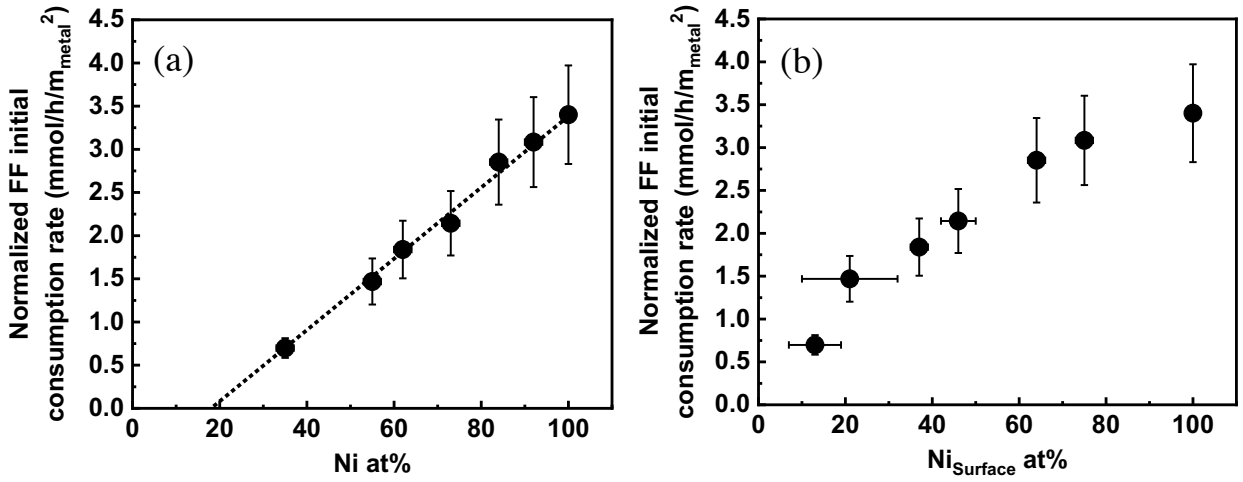

Figure 7. Initial rate of furfural consumption, normalized with respect to the exposed metal surface area, (a) as a function of the nominal Ni molar proportion; (b) as a function of the surface Ni molar proportion.

This initial rate was then plotted as a function of the surface Ni molar proportion, using the quantification results by LEIS and the error bars presented in section 3.5 (**Figure 7b**). When focusing on the composition of the outer shells of the Ni-Fe nanoparticles, the trend is not linear any more, with a steeper slope in the lower Ni proportion range. An extrapolation of the trend may indicate that a minimum of 10 Ni at% is required at the nanoparticles surface to catalyze hydrogenation. This pattern suggests that the hydrogenation of the aldehyde function is linked to the existence of ensembles of Ni atoms in Fe-rich areas, and that the impact of the growing connectivity between the neighboring Ni atoms is stronger at lower Ni content (high dilution of Ni with respect to Fe), and weaker at higher Ni contents (for which large Ni domains already exist). These results do not point to the existence of specific, isolated Ni-Fe sites that would perform the hydrogenation of the aldehyde function more rapidly on the bimetallic surfaces.

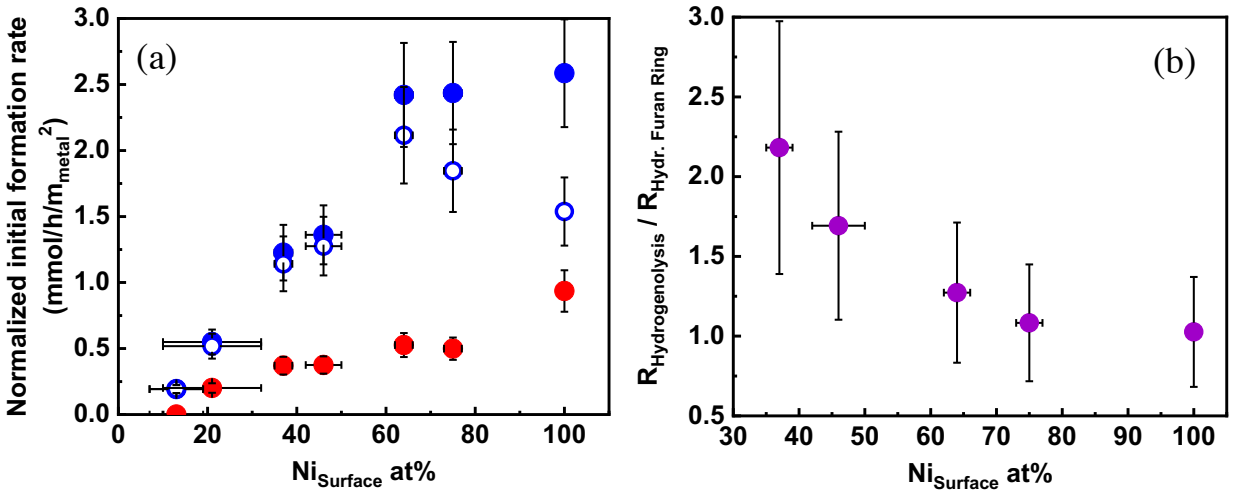

Figure 8. (a) Initial rate of products formation, normalized with respect to the exposed metal surface area, as a function of the surface Ni molar proportion. Full blue circles: FFA + iPrOMF; open blue circles: FFA alone; red circles: MF + THFFA + MTHF. (b) Ratio between the initial rate of hydrogenolysis and the initial rate of ring hydrogenation, as a function of the surface Ni molar proportion.

A comparison can be done with the influence of the surface Ni molar proportion on the formation rates of the different products. On **Figure 8a**, the products were grouped in two categories: those for which no secondary reaction with H_2 took place (FFA, iPrOMF; full blue circles); and those that underwent at least one step of hydrogenolysis or ring hydrogenation (MF, THFFA, MTHF; full red circles).

The pattern concerning the initial neat formation rate of FFA (as such, or under its ether form) is similar to the one found for the consumption of FF. Values seem to reach a plateau when the Ni proportion is high, as the consumption of FFA by hydrogenolysis or hydrogenation becomes prominent. Reaction rates of secondary processes involving H_2 also increase with the surface Ni molar proportion. A comparison between **Figures 7b** and **8a** shows that for $Ni_{55}Fe_{45}/SiO_2$, the ratio

between the rate of hydrogenation of the aldehyde function, and the total rate of the secondary hydroconversion processes, is 7. This ratio falls to 4 on the monometallic Ni catalyst, and ranges between 5 and 6 on the three intermediate systems. The extension of the Ni domains would thus favor the secondary processes of hydroconversion, in agreement with the fact that monometallic Ni is largely unselective. A more precise comparison is however difficult to make, because for Ni-rich catalysts the initial production of iPrOMF is not negligible at short reaction times, and the way its production interferes with the hydroconversion route is not known (for instance, how the ether function can act as a protecting group with respect to secondary reactions).

Given the preferential formation of MTHF from MF with respect to THFFA, it could be assumed that the conversion of molecules containing a furan ring, such as MF, was favored on Ni-rich surfaces. **Figure 8b** reports the ratio between the initial rate of the hydrogenolysis route (formation of MF) and the initial rate of the ring hydrogenation route (formation of THFFA and MTHF) as a function of the surface Ni molar proportion. The ring hydrogenation route is not favored on Fe-rich surfaces, whereas the two routes co-exist to a similar extent on Ni-rich surfaces.

The most selective Ni-Fe catalysts to FFA, those containing a nominal Ni molar proportion of 60 – 70 % and exhibiting a surface molar proportion of 35 – 45 Ni % only, would thus be characterized by the existence of active sites consisting of limited Ni ensembles, on which the hydrogenation of the aldehyde function of FF takes place at a moderate rate, hydrogenolysis of the oxygenated function takes place at a significantly slower rate, and the hydrogenation of the furan ring would be the slowest route of all. Enriching the Ni-Fe surface in Ni results in an increase of the three reaction rates, with a large impact on the secondary hydroconversion pathways, and especially the ring hydrogenation route. The size of Ni domains can influence the activation of the reactants in two respects: the organic molecules, through an adsorption either limited to the polar

function, or involving the furan ring when the size of the ensemble increases; and H_2, with a limitation of the amount of available H atoms. A comparison can be done with the distinction recently made in the literature between Ni edge and step sites, on which the hydrogenation of furfural would be limited to furfuryl alcohol, and flat Ni surfaces, on which the hydrogenation of the furan ring would be favored.[60-61][59,60] The existence of electronic effects in the bimetallic combinations cannot be excluded, but our observations do not provide conclusive elements on that point.

The gap on **Figure 8a** between the full blue circles (formation rate of FFA + iPrOMF) and the open blue circles (formation rate of FFA only) represents the initial formation rate of the ether, iPrOMF, which increases much when the Ni content increases in the catalyst. In contrast with the other pathways, etherification is expected to happen on unreduced metal ions acting as Lewis acidic centers rather than on metallic surfaces,[62-64][61–63] and a correlation with the surface Ni content is probably not relevant. The identification of unreduced Ni^{2+} ions as possible active sites for etherification may sound counterintuitive, as it was shown that Fe was the last metal to be reduced of the two, both during the initial reduction stage[23] and during re-activation in H_2, and that it was Ni that drove the reduction of Fe during re-activation (section 3.4, **Figures 5 and S6**). However, the role of Ni^{2+} ions is confirmed by the non-negligible etherification of THFFA to iPrOMTHF on the monometallic Ni catalyst (**Figure 6**, Ni_{100}/SiO_2, blue dotted line).

A minority of unreduced Ni^{2+} ions would not be detected by XAS, the only spectroscopy used here to follow the evolution of nickel, because the final XANES spectrum and EXAFS signal are dominated by the well-organized metallic phase. The reason why some Ni^{2+} ions would remain unreduced in the Ni-rich systems may be found in the poorer reducibility of Ni-rich phyllosilicates, compared to Ni-Fe-containing phases, as can be inferred from temperature-programmed reduction

profiles recorded on the solids after DPU synthesis (**Figure S13**). While the reduction of the metals is complete at 730 °C for $Ni_{55}Fe_{45}/SiO_2$, $Ni_{62}Fe_{38}/SiO_2$ and $Ni_{73}Fe_{27}/SiO_2$, it is not the case for $Ni_{84}Fe_{16}/SiO_2$, $Ni_{92}Fe_{8}/SiO_2$ and especially Ni_{100}/SiO_2 (one should be aware that the conditions of reduction for TPR and for the catalyst preparation are different, the latter involving a plateau at 700 °C, and that a direct extrapolation between the two reduction processes is not straightforward). Another hint can be found in the evolution of the specific surface area of the solids after reduction at 700 °C (**Table 1**). It first increases to a maximum value for $Ni_{62}Fe_{38}/SiO_2$ and $Ni_{73}Fe_{27}/SiO_2$, then decreases to reach a minimum for Ni_{100}/SiO_2. A similar pattern has been described for catalysts resulting from the precipitation of Ni- and Fe- containing hydrotalcites[16]. One can suppose that increasing the Ni global proportion has resulted in the formation of a more organized phyllosilicate phase, better crystallized and more difficult to reduce completely, compared with the mixed phyllosilicates containing a fraction of Fe larger than 20 %. The etherification pathway can be specific to catalysts prepared via an intermediate silicate phase, and may not be seen when using Ni-Fe/SiO_2 catalysts prepared by impregnation.

4. CONCLUSIONS

The hydroconversion of furfural in isopropanol was investigated using a series of Ni-Fe/SiO_2 and Ni/SiO_2 catalysts prepared by deposition-precipitation with urea, and differing by the molar proportions of the two metals in the Ni-Fe nanoparticles, from $Ni_{35}Fe_{65}$ to Ni_{100}. All catalysts exhibited *fcc* alloyed nanoparticles with similar size distribution (4 – 7 nm), similar metal dispersion (17 – 19 %), and a homogeneous composition throughout a given catalyst (standard deviation: 7 – 8 Ni at%).

Nevertheless, reduced Ni-Fe nanoparticles were all found to exhibit heterogeneities in their inner chemical order, and the nominal composition of the catalyst did not reflect the composition of the outer shells of the nanoparticles. A gradient of Ni concentration was found from a Ni-enriched core to Ni-depleted, Fe-enriched outer shells, with a Ni depletion of 20 % in average compared with the nominal composition, as determined from LEIS measurements. These outer shells readily oxidized upon exposure to dilute oxygen, but the Ni-Fe nanoparticles reverted to their former state upon re-activation in H_2 at 400 °C, and no permanent dealloying was observed. The reduction of the metals started at a lower temperature when the Ni proportion increased.

Fe-rich catalysts were poorly active in the hydrogenation of furfural, but selective in furfuryl alcohol. Increasing the overall Ni proportion to 60 – 75 Ni at%, and the related surface composition of the nanoparticles to 35 – 45 Ni at%, provided the highest yield of furfuryl alcohol in the experimental conditions of reaction. The active sites were supposed to consist of ensembles of Ni atoms, whose limited size would decrease the availability of H_2 and inhibit the planar adsorption of molecules possessing a furan ring compared to the adsorption via the terminal polar functions. Both the rate of hydrogenation of the aldehyde function of furfural, and the rate of secondary processes involving H_2 (hydrogenolysis of the alcohol function, hydrogenation of the furan ring) increased upon increasing the surface Ni proportion, the latter progressively gaining prominence with the formation of methylfuran, tetrahydrofurfuryl alcohol and methyltetrahydrofuran, which became the major product with the monometallic Ni catalyst. A high amount of Ni in the catalysts also favored side-reactions of etherification with isopropanol, possibly through the presence of residual Ni^{2+} ions coming from difficult-to-reduce, well-organized phyllosilicate phases formed during the synthesis by deposition-precipitation.

The composition of the outer shells of Ni-Fe nanoparticles is thus linked to the global composition of the Ni-Fe nanoparticles and evolves following a similar trend, but is not equal to it. More than specifically active surface sites or catalyst formulations, it is an adequate balance in the kinetics of the reactions enabled by the Ni ensembles located among Fe domains, that allows performing the hydrogenation of the aldehyde function of furfural, while limiting the reaction rate of secondary processes of hydrogenolysis and, especially, ring hydrogenation, linked to Ni-rich surfaces.

Supporting information

^{57}Fe Mössbauer spectra and data analysis for dried systems; X-ray diffractograms and data for catalysts reduced at 700 °C; bright-field TEM micrographs, size histograms and data; STEM-HAADF-HR-EELS images and data; X-ray absorption spectroscopy: spectra and data analysis for oxidation and re-activation experiments; ^{57}Fe Mössbauer data for re-activated systems; LEIS: Ni quantification profiles; reaction network in the hydroconversion of furfural; carbon balances and selectivities; recycling experiments: catalytic data, bright-field TEM micrographs and size histograms, LEIS spectra; temperature-reduction profiles and data analysis.

Corresponding Author

* Dr. Eric Marceau, eric.marceau@univ-lille.fr

Present Addresses

† Unité de Chimie Environnementale et Interactions sur le Vivant (UCEIV, EA 4492), SFR Condorcet FR CNRS 3417, Université du Littoral Côte d'Opale (ULCO), 145 Av. M. Schumann, Dunkerque, 59140, France

Author Contributions

The manuscript was written through contributions of all authors. D. S. was a PhD candidate who prepared the catalysts, characterized them by XRD, TEM, N_2 physisorption and TPR, performed the catalytic tests, and wrote the first draft of the manuscript. A. S. was a post-doctoral fellow who performed the recycling experiments. J. S. G., C. C. and E. M. participated in the *in situ* XAS measurements, headed by C. L. F. at synchrotron SOLEIL. A. S. M. performed the LEIS measurements and analyzed the data. M. M. performed the STEM-HR-EELS measurements and analyzed the data. L. S. analyzed the Mössbauer spectra and wrote the corresponding sections. M. T. S. recorded the Mössbauer spectra. R. W., S. P. and E. M. were supervisors to D. S. and A. S., and all three contributed to the revision of the catalysis sections. R. W. and S. P. supervised the catalytic tests and analysis by XRF. E. M. analyzed the XAS data, wrote the corresponding sections, revised the characterization sections and performed the complete revision of the manuscript in its final form. All authors have given approval to the final version of the manuscript.

Funding Sources

This work has benefited from the support of the CSC-Centrale Lille PhD scholarship program (D. S.) and of the French National Research Agency (ANR), through the NobleFreeCat project (ANR-17-CE07-0022).

The Chevreul Institute and the TEM facility in Lille are thanked for their help in the development of this work through the ARCHI-CM project supported by the “Ministère de l’Enseignement Supérieur de la Recherche et de l’Innovation”, the region “Hauts-de-France”, the ERDF program of the European Union and the “Métropole Européenne de Lille”.

XAS experiments were performed on the ROCK beamline, using the Chemistry support lab, at SOLEIL Synchrotron, France (beamtime allocated for proposal numbers 20151218 and 20161106). The ROCK beamline at synchrotron SOLEIL is benefiting from a public grant overseen by the French National Research Agency as a part of the 'Investissements d'Avenir' program (PIA) with the contractual reference 'ANR-10-EQPX-45'.

The REALCAT platform is benefitting from a state subsidy administrated by the French National Research Agency within the frame of the 'Future Investments' program (PIA), with the contractual reference 'ANR-11-EQPX-0037'. The European Union, through the ERDF funding administered by the Hauts-de-France Region, has co-financed the platform. Centrale Lille, the CNRS, and University of Lille as well as the Centrale Initiatives Foundation, are thanked for their financial contributions to the acquisition and implementation of the equipment.

The "Réseau des Rayons X et Gamma" (Univ. Montpellier, France) is gratefully thanked for granting access to their Mössbauer spectroscopy platform. Joelle Thuriot-Roukos (XRF, ICP-OES), Olivier Gardoll (TPR), Svetlana Heyte (SPR/GC-MS) and Jérémy Dhainaut (bright-field TEM measurements), all at UCCS, are thanked for their help.

The authors declare no competing interests.

REFERENCES

(1) Brownlee, H. J.; Miner, C. S. Industrial Development of Furfural. *Ind. Eng. Chem.* **1948**, *40*, 201–204. https://doi.org/10.1021/ie50458a005.

(2) Yan, K.; Wu, G.; Lafleur, T.; Jarvis, C. Production, Properties and Catalytic Hydrogenation of Furfural to Fuel Additives and Value-Added Chemicals. *Renew. Sustain. Energy Rev.* **2014**, *38*, 663–676. https://doi.org/10.1016/j.rser.2014.07.003.

(3) Li, X.; Jia, P.; Wang, T. Furfural: A Promising Platform Compound for Sustainable Production of C4 and C5 Chemicals. *ACS Catal.* **2016**, *6*, 7621–7640. https://doi.org/10.1021/acscatal.6b01838.

(4) Chen, S.; Wojcieszak, R.; Dumeignil, F.; Marceau, E.; Royer, S. How Catalysts and Experimental Conditions Determine the Selective Hydroconversion of Furfural and 5-Hydroxymethylfurfural. *Chem. Rev.* **2018**, *118*, 11023–11117. https://doi.org/10.1021/acs.chemrev.8b00134.

(5) Halilu, A.; Ali, T. H.; Atta, A. Y.; Sudarsanam, P.; Bhargava, S. K.; Abd Hamid, S. B. Highly Selective Hydrogenation of Biomass-Derived Furfural into Furfuryl Alcohol Using a Novel Magnetic Nanoparticles Catalyst. *Energy and Fuels* **2016**, *30*, 2216–2226. https://doi.org/10.1021/acs.energyfuels.5b02826.

(6) Liu, L.; Liu, H.; Huang, W.; He, Y.; Zhang, W.; Wang, C.; Lin, H. Mechanism and Kinetics of the Electrocatalytic Hydrogenation of Furfural to Furfuryl Alcohol. *J. Electroanal. Chem.* **2017**, *804*, 248–253. https://doi.org/10.1016/j.jelechem.2017.09.021.

(7) Li, H.; Luo, H.; Zhuang, L.; Dai, W.; Qiao, M. Liquid Phase Hydrogenation of Furfural to Furfuryl Alcohol over the Fe-Promoted Ni-B Amorphous Alloy Catalysts. *J. Mol. Catal. A Chem.* **2003**, *203*, 267–275. https://doi.org/10.1016/S1381-1169(03)00368-6.

(8) Nguyen-Huy, C.; Kim, J. S.; Yoon, S.; Yang, E.; Kwak, J. H.; Lee, M. S.; An, K. Supported Pd Nanoparticle Catalysts with High Activities and Selectivities in Liquid-Phase Furfural Hydrogenation. *Fuel* **2018**, *226*, 607–617. https://doi.org/10.1016/j.fuel.2018.04.029.

(9) Goh, T. W.; Tsung, C. K.; Huang, W. Spectroscopy Identification of the Bimetallic Surface of Metal-Organic Framework-Confined Pt-Sn Nanoclusters with Enhanced Chemoselectivity in Furfural Hydrogenation. *ACS Appl. Mater. Interfaces* **2019**, *11*, 23254–23260. https://doi.org/10.1021/acsami.9b06229.

(10) Lee, J.; Woo, J.; Nguyen-Huy, C.; Lee, M. S.; Joo, S. H.; An, K. Highly Dispersed Pd Catalysts Supported on Various Carbons for Furfural Hydrogenation. *Catal. Today* **2020**, *350*, 71–79. https://doi.org/10.1016/j.cattod.2019.06.032.

(11) Yan, H.; Lv, H.; Yi, H.; Liu, W.; Xia, Y.; Huang, X.; Huang, W.; Wei, S.; Wu, X.; Lu, J. Understanding the Underlying Mechanism of Improved Selectivity in Pd_1 Single-Atom Catalyzed Hydrogenation Reaction. *J. Catal.* **2018**, *366*, 70–79. https://doi.org/10.1016/j.jcat.2018.07.033.

(12) Pirmoradi, M.; Kastner, J. R. A Kinetic Model of Multi-Step Furfural Hydrogenation over a Pd-TiO_2 Supported Activated Carbon Catalyst. *Chem. Eng. J.* **2021**, *414*, 128693. https://doi.org/https://doi.org/10.1016/j.cej.2021.128693.

(13) Li, S.; Dong, M.; Yang, J.; Cheng, X.; Shen, X.; Liu, S.; Wang, Z. Q.; Gong, X. Q.; Liu, H.; Han, B. Selective Hydrogenation of 5-(Hydroxymethyl)Furfural to 5-Methylfurfural over Single Atomic Metals Anchored on Nb_2O_5. *Nat. Commun.* **2021**, *12*, 584. https://doi.org/10.1038/s41467-020-20878-7.

(14) Jiménez-Gómez, C. P.; Defilippi, C.; Cecilia, J. A.; Moreno-Tost, R.; Maireles-Torres, P.; Giordano, C. The Role of Nitride Species in the Gas-Phase Furfural Hydrogenation Activity

of Supported Nickel Catalysts. *Mol. Catal.* **2020**, *487*, 110889. https://doi.org/https://doi.org/10.1016/j.mcat.2020.110889.

(15) Xu, J.; Cui, Q.; Xue, T.; Guan, Y.; Wu, P. Total Hydrogenation of Furfural under Mild Conditions over a Durable Ni/TiO_2–SiO_2 Catalyst with Amorphous TiO_2 Species. *ACS Omega* **2020**, *5*, 30257–30266. https://doi.org/10.1021/acsomega.0c04736.

(16) Shao, Y.; Wang, J.; Sun, K.; Gao, G.; Li, C.; Zhang, L.; Zhang, S.; Xu, L.; Hu, G.; Hu, X. Selective Hydrogenation of Furfural and Its Derivative over Bimetallic NiFe-Based Catalysts: Understanding the Synergy between Ni Sites and Ni–Fe Alloy. *Renew. Energy* **2021**, *170*, 1114–1128. https://doi.org/https://doi.org/10.1016/j.renene.2021.02.056.

(17) Pomeroy, B.; Grilc, M.; Gyergyek, S.; Likozar, B. Catalyst Structure-Based Hydroxymethylfurfural (HMF) Hydrogenation Mechanisms, Activity and Selectivity over Ni. *Chem. Eng. J.* **2021**, *412*, 127553. https://doi.org/https://doi.org/10.1016/j.cej.2020.127553.

(18) Sunyol, C.; English Owen, R.; González, M. D.; Salagre, P.; Cesteros, Y. Catalytic Hydrogenation of Furfural to Tetrahydrofurfuryl Alcohol Using Competitive Nickel Catalysts Supported on Mesoporous Clays. *Appl. Catal. A Gen.* **2021**, *611*, 117903. https://doi.org/https://doi.org/10.1016/j.apcata.2020.117903.

(19) Chen, S. H.; Tseng, Y. C.; Yang, S. C.; Lin, S. D. Investigating Hydrogenation and Decarbonylation in Vapor-Phase Furfural Hydrotreating over Ni/SiO_2 Catalysts: Propylene Production. *Appl. Catal. A Gen.* **2021**, *613*, 118020. https://doi.org/https://doi.org/10.1016/j.apcata.2021.118020.

(20) Yu, X.; Chen, J.; Ren, T. Promotional Effect of Fe on Performance of Ni/SiO_2 for Deoxygenation of Methyl Laurate as a Model Compound to Hydrocarbons. *RSC Adv.* **2014**, *4*, 46427–46436. https://doi.org/10.1039/c4ra07932a.

(21) Putro, W. S.; Kojima, T.; Hara, T.; Ichikuni, N.; Shimazu, S. Selective Hydrogenation of Unsaturated Carbonyls by Ni-Fe-Based Alloy Catalysts. *Catal. Sci. Technol.* **2017**, *7*, 3637–3646. https://doi.org/10.1039/c7cy00945c.

(22) Jiménez-Gómez, C. P.; Cecilia, J. A.; García-Sancho, C.; Moreno-Tost, R.; Maireles-Torres, P. Selective Production of Furan from Gas-Phase Furfural Decarbonylation on Ni-MgO Catalysts. *ACS Sustain. Chem. Eng.* **2019**, *7*, 7676–7685. https://doi.org/10.1021/acssuschemeng.8b06155.

(23) Shi, D.; Yang, Q.; Peterson, C.; Lamic-Humblot, A. F.; Girardon, J. S.; Griboval-Constant, A.; Stievano, L.; Sougrati, M. T.; Briois, V.; Bagot, P. A. J.; Wojcieszak, R.; Paul, S.; Marceau, E. Bimetallic Fe-Ni/SiO_2 Catalysts for Furfural Hydrogenation: Identification of the Interplay between Fe and Ni during Deposition-Precipitation and Thermal Treatments. *Catal. Today* **2019**, *334*, 162–172. https://doi.org/10.1016/j.cattod.2018.11.041.

(24) Chieffi, G.; Giordano, C.; Antonietti, M.; Esposito, D. FeNi Nanoparticles with Carbon Armor as Sustainable Hydrogenation Catalysts: Towards Biorefineries. *J. Mater. Chem. A* **2014**, *2*, 11591–11596. https://doi.org/10.1039/c4ta02457e.

(25) Jia, P.; Lan, X.; Li, X.; Wang, T. Highly Active and Selective NiFe/SiO_2 Bimetallic Catalyst with Optimized Solvent Effect for the Liquid-Phase Hydrogenation of Furfural to Furfuryl Alcohol. *ACS Sustain. Chem. Eng.* **2018**, *6*, 13287–13295. https://doi.org/10.1021/acssuschemeng.8b02876.

(26) Jia, P.; Lan, X.; Li, X.; Wang, T. Highly Selective Hydrogenation of Furfural to Cyclopentanone over a NiFe Bimetallic Catalyst in a Methanol/Water Solution with a Solvent Effect. *ACS Sustain. Chem. Eng.* **2019**, *7*, 15221–15229. https://doi.org/10.1021/acssuschemeng.9b02112.

(27) Sitthisa, S.; An, W.; Resasco, D. E. Selective Conversion of Furfural to Methylfuran over Silica-Supported NiFe Bimetallic Catalysts. *J. Catal.* **2011**, *284*, 90–101. https://doi.org/https://doi.org/10.1016/j.jcat.2011.09.005.

(28) Wang, C.; Luo, J.; Liao, V.; Lee, J. D.; Onn, T. M.; Murray, C. B.; Gorte, R. J. A Comparison of Furfural Hydrodeoxygenation over Pt-Co and Ni-Fe Catalysts at High and Low H_2 Pressures. *Catal. Today* **2018**, *302*, 73–79. https://doi.org/https://doi.org/10.1016/j.cattod.2017.06.042.

(29) Shi, D.; Wojcieszak, R.; Paul, S.; Marceau, E. Ni Promotion by Fe: What Benefits for Catalytic Hydrogenation? *Catalysts* **2019**, *9*, 451–477. https://doi.org/10.3390/catal9050451.

(30) Yu, W.; Xiong, K.; Ji, N.; Porosoff, M. D.; Chen, J. G. Theoretical and Experimental Studies of the Adsorption Geometry and Reaction Pathways of Furfural over FeNi Bimetallic Model Surfaces and Supported Catalysts. *J. Catal.* **2014**, *317*, 253–262. https://doi.org/https://doi.org/10.1016/j.jcat.2014.06.025.

(31) Liu, X.; An, W.; Turner, C. H.; Resasco, D. E. Hydrodeoxygenation of M-Cresol over Bimetallic NiFe Alloys: Kinetics and Thermodynamics Insight into Reaction Mechanism. *J. Catal.* **2018**, *359*, 272–286. https://doi.org/https://doi.org/10.1016/j.jcat.2018.01.006.

(32) Nie, L.; de Souza, P. M.; Noronha, F. B.; An, W.; Sooknoi, T.; Resasco, D. E. Selective Conversion of M-Cresol to Toluene over Bimetallic Ni–Fe Catalysts. *J. Mol. Catal. A*

Chem. **2014**, *388–389*, 47–55. https://doi.org/https://doi.org/10.1016/j.molcata.2013.09.029.

(33) Jiang, Z.; Wan, W.; Lin, Z.; Xie, J.; Chen, J. G. Understanding the Role of M/Pt(111) (M = Fe, Co, Ni, Cu) Bimetallic Surfaces for Selective Hydrodeoxygenation of Furfural. *ACS Catal*. **2017**, *7*, 5758–5765. https://doi.org/10.1021/acscatal.7b01682.

(34) Kumbhar, P. S.; Kharkar, M. R.; Yadav, G. D.; Rajadhyaksha, R. A. Geometric and Electronic Effects in Silica Supported Bimetallic Nickel-Copper and Nickel-Iron Catalysts for Liquid-Phase Hydrogenation of Acetophenone and Benzonitrile. *J. Chem. Soc. Chem. Commun.* **1992**, *7*, 584–586. https://doi.org/10.1039/C39920000584.

(35) Unmuth, E. E.; Schwartz, L. H.; Butt, J. B. Iron Alloy Fischer-Tropsch Catalysts: I. Oxidation-reduction Studies of the Fe-Ni system. *J. Catal.* **1980**, *61*, 242–255. https://doi.org/10.1016/0021-9517(80)90360-7.

(36) Tomishige, K.; Li, D.; Tamura, M.; Nakagawa, Y. Nickel-Iron Alloy Catalysts for Reforming of Hydrocarbons: Preparation, Structure, and Catalytic Properties. *Catal. Sci. Technol.* **2017**, *7*, 3952–3979. https://doi.org/10.1039/c7cy01300k.

(37) Mutz, B.; Belimov, M.; Wang, W.; Sprenger, P.; Serrer, M. A.; Wang, D.; Pfeifer, P.; Kleist, W.; Grunwaldt, J. D. Potential of an Alumina-Supported Ni_3Fe Catalyst in the Methanation of CO_2: Impact of Alloy Formation on Activity and Stability. *ACS Catal.* **2017**, *7*, 6802–6814. https://doi.org/10.1021/acscatal.7b01896.

(38) Han, Q.; Ur Rehman, M.; Wang, J.; Rykov, A.; Gutiérrez, O.Y.; Zhao, Y.; Wang, Sh.; Ma, X.; Lercher, J.A. The synergistic effect between Ni sites and Ni-Fe alloy sites on hydrodeoxygenation of lignin-derived phenols. *Appl. Catal. B. Env*. **2019**, *253*, 348-358. https://doi.org/10.1016/j.apcatb.2019.04.065

(39) Margossian, T.; Larmier, K.; Kim, S. M.; Krumeich, F.; Müller, C.; Copéret, C. Supported Bimetallic NiFe Nanoparticles through Colloid Synthesis for Improved Dry Reforming Performance. *ACS Catal*. **2017**, *7*, 6942–6948. https://doi.org/10.1021/acscatal.7b02091.

(40) Briois, V.; La Fontaine, C.; Belin, S.; Barthe, L.; Moreno, T.; Pinty, V.; Carcy, A.; Girardot, R.; Fonda, E. ROCK: The New Quick-EXAFS Beamline at SOLEIL. *J. Phys. Conf. Ser.* **2016**, *712*, 12149. https://doi.org/10.1088/1742-6596/712/1/012149.

(41) Fonda, E.; Rochet, A.; Ribbens, M.; Barthe, L.; Belin, S.; Briois, V. The SAMBA Quick-EXAFS Monochromator: XAS with Edge Jumping. *J. Synchrotron Radiat.* **2012**, *19*, 417–424. https://doi.org/https://doi.org/10.1107/S0909049512009703.

(42) Lesage, C.; Devers, E.; Legens, C.; Fernandes, G.; Roudenko, O.; Briois, V. High Pressure Cell for Edge Jumping X-Ray Absorption Spectroscopy: Applications to Industrial Liquid Sulfidation of Hydrotreatment Catalysts. *Catal*. *Today* **2019**, *336*, 63–73. https://doi.org/https://doi.org/10.1016/j.cattod.2019.01.081.

(43) Cassinelli, W. H.; Martins, L.; Passos, A. R.; Pulcinelli, S. H.; Santilli, C. V.; Rochet, A.; Briois, V. Multivariate Curve Resolution Analysis Applied to Time-Resolved Synchrotron X-Ray Absorption Spectroscopy Monitoring of the Activation of Copper Alumina Catalyst. *Catal. Today* **2014**, *229*, 114–122. https://doi.org/10.1016/j.cattod.2013.10.077.

(44) Hong, J.; Marceau, E.; Khodakov, A. Y.; Gaberová, L.; Griboval-Constant, A.; Girardon, J. S.; La Fontaine, C.; Briois, V. Speciation of Ruthenium as a Reduction Promoter of Silica-Supported Co Catalysts: A Time-Resolved in Situ XAS Investigation. *ACS Catal.* **2015**, *5*, 1273–1282. https://doi.org/10.1021/cs501799p.

(45) Rochet, A.; Baubet, B.; Moizan, V.; Pichon, C.; Briois, V. Co-K and Mo-K Edges Quick-XAS Study of the Sulphidation Properties of Mo/Al_2O_3 and $CoMo/Al_2O_3$ Catalysts. *Comptes Rendus Chim.* **2016**, *19*, 1337–1351. https://doi.org/10.1016/j.crci.2016.01.009.

(46) Jaumot, J.; de Juan, A.; Tauler, R. MCR-ALS GUI 2.0: New Features and Applications. *Chemom. Intell. Lab. Syst.* **2015**, *140*, 1–12. https://doi.org/https://doi.org/10.1016/j.chemolab.2014.10.003.

(47) Ravel, B.; Newville, M. ATHENA, ARTEMIS, HEPHAESTUS: Data Analysis for X-Ray Absorption Spectroscopy Using IFEFFIT. *J. Synchrotron Radiat.* **2005**, *12*, 537–541. https://doi.org/10.1107/S0909049505012719.

(48) Newville, M. IFEFFIT: Interactive XAFS Analysis and FEFF Fitting. *J. Synchrotron Rad.* **2001**, *8*, 322–324. https://doi.org/10.1107/S0909049500016964.

(49) Sadier, A.; Shi, D.; Mamede, A. S.; Paul, S.; Marceau, E.; Wojcieszak, R. Selective Aqueous Phase Hydrogenation of Xylose to Xylitol over SiO_2-Supported Ni and Ni-Fe Catalysts: Benefits of Promotion by Fe. *Appl. Catal. B Environ.* **2021**, *298*, 120564. https://doi.org/10.1016/j.apcatb.2021.120564.

(50) Chernysh, V. S.; Brongersma, H. H.; Brüner, P.; Grehl, T. Surface Composition of Ion Bombarded Nickel Based Alloys. *Nucl. Instruments Methods Phys. Res. Sect. B Beam Interact. with Mater. Atoms* **2019**, *460*, 180–184. https://doi.org/https://doi.org/10.1016/j.nimb.2019.02.008.

(51) Ashok, J.; Kawi, S. Nickel–Iron Alloy Supported over Iron–Alumina Catalysts for Steam Reforming of Biomass Tar Model Compound. *ACS Catal*. **2014**, *4*, 289–301. https://doi.org/10.1021/cs400621p.

(52) Gil, A.; Díaz, A.; Gandía, L. M.; Montes, M. Influence of the Preparation Method and the Nature of the Support on the Stability of Nickel Catalysts. *Appl. Catal. A, Gen.* **1994**, *109*, 167–179. https://doi.org/10.1016/0926-860X(94)80116-9.

(53) Marceau, E.; Löfberg, A.; Giraudon, J. M.; Négrier, F.; Che, M.; Leclercq, L. From Al_2O_3-Supported Ni(II)-Ethylenediamine Complexes to CO Hydrogenation Catalysts: Characterization of the Surface Sites and Catalytic Properties. *Appl. Catal. A Gen.* **2009**, *362*, 34–39. https://doi.org/10.1016/j.apcata.2009.04.029.

(54) Johnson, C. E.; Ridout, M. S.; Cranshaw, T. E. The Mössbauer Effect in Iron Alloys. *Proc. Phys. Soc.* **1963**, *81*, 1079–1090. https://doi.org/10.1088/0370-1328/81/6/313.

(55) Nagorny, K.; Bubert, S. Mössbauer Spectroscopic Investigations of Bimetallic FeCo, FeNi, and FeRu Model Catalysts Supported on Magnesium Hydroxide Carbonate. *J. Catal.* **1987**, *108*, 112–134. https://doi.org/https://doi.org/10.1016/0021-9517(87)90159-X.

(56) Wang, L.; Li, D.; Koike, M.; Koso, S.; Nakagawa, Y.; Xu, Y.; Tomishige, K. Catalytic Performance and Characterization of Ni-Fe Catalysts for the Steam Reforming of Tar from Biomass Pyrolysis to Synthesis Gas. *Appl. Catal. A Gen.* **2011**, *392*, 248–255. https://doi.org/https://doi.org/10.1016/j.apcata.2010.11.013.

(57) Rao, Z.; Cao, Y.; Huang, Z.; Yin, Z.; Wan, W.; Ma, M.; Wu, Y.; Wang, J.; Yang, G.; Cui, Y.; Gong, Z.; Zhou, Y. Insights into the Nonthermal Effects of Light in Dry Reforming of Methane to Enhance the H_2/CO Ratio near Unity over Ni/Ga_2O_3. *ACS Catal.* **2021**, *11*, 4730–4738. https://doi.org/10.1021/acscatal.0c04826.

(58) Mizushima, T.; Tohji, K.; Udagawa, Y.; Harada, M.; Ishikawa, M.; Ueno, A. Characterization of Silica-Supported Bimetallic Iron-Nickel Catalysts by EXAFS. *J. Catal.* **1988**, *112*, 282–289. https://doi.org/https://doi.org/10.1016/0021-9517(88)90140-6.

(59) Fang, H.; Zheng, J.; Luo, X.; Du, J.; Roldan, A.; Leoni, S.; Yuan, Y. Product Tunable Behavior of Carbon Nanotubes-Supported Ni–Fe Catalysts for Guaiacol Hydrodeoxygenation. *Appl. Catal. A Gen.* **2017**, *529*, 20–31. https://doi.org/https://doi.org/10.1016/j.apcata.2016.10.011.

(60) Meng, X.; Yang, Y.; Chen, L.; Xu, M.; Zhang, X.; Wei, M. A Control over Hydrogenation Selectivity of Furfural via Tuning Exposed Facet of Ni Catalysts. *ACS Catal*. **2019**, *9*, 4226–4235. https://doi.org/10.1021/acscatal.9b00238.

(61) Chen, L.; Ye, J.; Yang, Y.; Yin, P.; Feng, H.; Chen, C.; Zhang, X.; Wei, M.; Truhlar, D. G. Catalytic Conversion Furfuryl Alcohol to Tetrahydrofurfuryl Alcohol and 2-Methylfuran at Terrace, Step, and Corner Sites on Ni. *ACS Catal.* **2020**, *10*, 7240–7249. https://doi.org/10.1021/acscatal.0c01441.

(62) Li, X. L.; Zhang, K.; Chen, S. Y.; Li, C.; Li, F.; Xu, H. J.; Fu, Y. A Cobalt Catalyst for Reductive Etherification of 5-Hydroxymethyl-Furfural to 2,5-Bis(Methoxymethyl)Furan under Mild Conditions. *Green Chem.* **2018**, *20*, 1095–1105. https://doi.org/10.1039/C7GC03072J.

(63) Koehle, M.; Lobo, R. F. Lewis Acidic Zeolite Beta Catalyst for the Meerwein-Ponndorf-Verley Reduction of Furfural. *Catal. Sci. Technol.* **2016**, *6*, 3018–3026. https://doi.org/10.1039/c5cy01501d.

(64) Natsir, T. A.; Shimazu, S. Fuels and Fuel Additives from Furfural Derivatives via Etherification and Formation of Methylfurans. *Fuel Process. Technol.* **2020**, *200*, 106308. https://doi.org/https://doi.org/10.1016/j.fuproc.2019.106308.